INVESTIGATION OF ANISOTROPIC HEAT TRANSPORT THROUGH FREQUENCY DOMAIN THERMOREFLECTANCE TECHNIQUE

MIZANUR RAHMAN

A THESIS SUBMITTED TO

THE FACULTY OF GRADUATE STUDIES

IN PARTIAL FULFILLMENT OF THE REQUIREMENTS

FOR THE DEGREE OF

MASTER OF SCIENCE

GRADUATE PROGRAM IN PHYSICS AND ASTRONOMY

YORK UNIVERSITY

TORONTO, ONTARIO

APRIL 2019

ABSTRACT

Thermophysical properties of thin film materials are of great importance for thermal management in devices including transistors, lasers, sensors, and plasmonic structures. In this thesis, I examine the characterization of heat transport in anisotropic materials through frequency domain thermoreflectance (FDTR) technique. Firstly, I describe the experimental setup and numerical modeling of the FDTR. Then, I explain the development of beam offset frequency domain thermoreflectance (BO-FDTR) and frequency domain magneto-optical Kerr effect (FD-MOKE) used to measure the anisotropic thermal properties with enhanced sensitivity. Monte Carlo computational method is also explained for uncertainty calculations. Finally, the demonstrations of measuring in-plane and out-of-plane thermal conductivities, and thermal boundary conductance with the metallic layer of anisotropic materials including 2D layered materials and printed films made of 2D-materials based inks are discussed. The measured thermal properties will be helpful for device applications that take advantage of the promising qualities of emerging 2D materials.

ACKNOWLEDGMENTS

First of all, I would like to express my gratitude to Professor Simone Pisana for being a dedicated supervisor, very helpful mentor and for his invaluable support. He is truly inspirational, very dedicated to his students, always available and willing to help. I want to offer special thanks to the member of my supervisory committee Professor Gerd Grau for his valuable time and guidance. I am grateful to Professor Paul O'Brien for his valuable time. I also like to thank Prof. Stephan Hofmann, Dr. P. Braeuninger-Weimer at the University of Cambridge, Prof. Cinzia Casiraghi, Dr. K. Parvez, and Dr. C. Dun at the University of Manchester, and Prof. Olav Hellwig at the Technical University Chemnitz for their contributions to our publications. Without their help, much of the work in this thesis would not have been possible. I also thank Dr. Henry Lee, Dr. Jared Mudrik, Harlan Kuntz at the University of Toronto and Calvin Pettinger at York University for their help during nanofabrication and materials characterization. I owe special thanks to my lab mates Mohammadreza Shahzadeh, Shany Mary Oommen, and Olga Andriyevska for a pleasant and collaborating environment in the Heated Lab and their support. Finally, I am very grateful to my friends and family members for their unconditional love and support.

TABLE OF CONTENTS

Abstract ii

Acknowledgments iii

Table of Contents iv

List of Tables vii

List of figures viii

Chapter 1 : Introduction and Background 1

1.1 Thermal Boundary Conductance 2

1.1.1 Acoustic Mismatch Model 4

1.1.2 Diffuse Mismatch Model 5

1.2 Techniques for Thermal Measurement 6

1.3 Anisotropy 8

1.4 Two Dimensional (2D) Materials 11

1.5 Solution Processed (2D) Materials 12

1.6 Organization of the Thesis 13

Chapter 2 : Frequency Domain Thermoreflectance (FDTR) 15

2.1 Overview 15

2.2 Difference Between TDTR and FDTR 15

2.3 Analytical Modelling 17

2.4 Sensitivity 20

2.5 Experimental System 23

2.6 Spot Size Measurement 25

2.7 Monte Carlo Computational Method for Uncertainty Calculation 26
2.8 Summary 28
Chapter 3 : Thermal Transport in Anisotropic Materials Through Beam Offset FDTR 29
3.1 Overview 29
3.2 Sample Preparation 31
3.3 Theory and Sensitivity Analysis 32
3.4 Experimental Method for Beam-offset FDTR 37
3.5 Results and Discussions 39
3.6 Summary 46
Chapter 4 : Thermal Transport in 2D Materials Through FD-MOKE 47
4.1 Overview 47
4.2 FD-MOKE 48
4.3 Sample Preparation and Materials Characterization 50
4.4 Sensitivity Analysis 53
4.5 Experimental Method 55
4.6 Uncertainty Estimation 58
4.7 Results and Discussions 60
4.8 Summary 67
Chapter 5 : Thermal Transport in Printed Films of 2D Inks 68
5.1 Overview 68
5.2 Sample Preparation and Sensitivity Analysis 69
5.3 Thermal Conductivity Measurements 72
5.4 Results and Discussions 73

5.5 Summary 86

Chapter 6 : Conclusion and Outlook 87

6.1 Summary of the thesis 87

6.2 Outlook 89

References 90

LIST OF TABLES

Table 3. 1 Nominal values for fitting and sensitivity analysis. Thickness values are obtained by white light interferometry or X-Ray reflectivity. The K for Al is assumed isotropic and determined by four point probe. *: the value of K for Al for these samples may have been affected by small grain sizes and the presence of residual oxygen in the deposition chamber. Blank values indicate a property that was obtained from fits to the experimental data. 36

Table 3. 2 Measured values for different anisotropic samples. *: the error bar here represents the confidence interval obtained from 9 measurements. †: the TBC in this case is that of the Al/Graphene/SiO_2 structure. 40

Table 4. 1 Measured values for different samples. [a]: The error bar here represents the standard deviation obtained from Monte Carlo simulations. [b]: the TBC, in this case is across the Ni/sample/SiO_2 interfaces. 62

LIST OF FIGURES

Figure 2. 1 depicts the sensitivity to $K_{\parallel}$ (dash lines) and $K_{\perp}$ (solid lines) of (a) Si for the Al (50nm) / Si structure and (b) graphite for the Al (50nm) / graphite structure for several RMS spot sizes. 21

Figure 2. 2 (a) FDTR Setup. (b) Experimental phase data with analytical fit on Al/SiO_2/Si sample structure with modulation up to ~100 MHz. 23

Figure 2. 3 Pump spot size measurement 25

Figure 2. 4 Histogram from Monte Carlo simulation. The resulting value for $K_{\parallel}$ is 270 ± 28.2 W/mK 27

Figure 3. 1 The probe beam is focused at an offset X_0. 32

Figure 3. 2 (a) and (b) depict the sensitivity of the measured thermal phase to changes in various parameters at 0 μm and 2 μm beam offsets respectively, (c) and (d) show the sensitivities to in-plane and out-of-plane thermal conductivity of Graphite, respectively, for several values of beam offsets. 34

Figure 3. 3 Schematic diagram of beam-offset FDTR 37

Figure 3. 4 (a) Experimental phase data (symbols) with fitted analytical solution (solid line) on the Al/Graphite sample at 2 μm beam offset. For comparison, the dashed line is the model prediction for the same structure, but without the TBC present at the Al/Graphite interface. Panel (b) shows aggregate data and global fit using 3 beam offset values: 0 μm (black), 1.5 μm (red) and 2 μm (navy). 39

Figure 3. 5 (a): Sensitivity to $K_{\perp}$, $K_{\parallel}$ of c-Sapphire and TBC across Al/c- Sapphire interfaces, for several values of beam offsets. (b) Experimental phase data (symbols) with fitted analytical solution (solid lines) for the Al/c- Sapphire sample. The beam offset values were 1 μm (black), 1.5 μm (red) and 2 μm(navy). 41

Figure 3. 6 (a) Experimental phase data at 0 μm beam offset for the Al/Graphene/SiO_2/Si sample on an area containing Graphene (black symbols) compared with an area that does not contain Graphene (red symbols). (b): Sensitivity to $K_{\perp}$ of Graphene and TBC across Al/Graphene/SiO_2 interfaces for the Al/Graphene/SiO_2/Si sample, for several values of beam offsets of 1 μm (black), 1.5 μm red) and 2 μm (navy). (c): Experimental phase data (symbols) with fitted analytical solution (solid lines) for the

Al/Graphene/SiO_2/Si sample. The beam-offset values were 0 μm (black), 1 μm (red) and 1.5 μm (navy). (d): $K_{\parallel}$ of single layer Graphene for the structure Al/Graphene/SiO_2/Si extracted from different locations in the sample. 42

Figure 4. 1 Measured Raman Spectra of the 2D materials in this study 51

Figure 4. 2 (a) and (b) plot the sensitivity of the measured thermal phase to the in-plane thermal conductivity of single-layer graphene and the TBC across the Ni/graphene/SiO_2 interfaces for several values of the transducer thickness. (c) and (d) show the sensitivity to the measured thermal phase to changes in different parameter using a 20nm Ni transducer. 53

Figure 4. 3 Schematic diagram of the Frequency Domain Magneto-Optical Kerr Effect setup 55

Figure 4. 4 Monte Carlo histograms for the 20-layer h-BN sample 58

Figure 4. 5 Panels (a), (b), and (c) show aggregate data (symbols) and global fit (solid lines) using 2 beam offset values: 1 μm (black) and 1.5 μm (red) for the Ni/graphene(1L)/SiO_2/Si, Ni/h-BN(4L)/SiO_2/Si, and Ni/MoS_2(2L)/SiO_2/Si samples, respectively. (d) data and fit at 1 μm offset for the Ni/$MoSe_2$ crystal (black) and at 0 μm offset for Ni/native SiO_2/Si (red) samples, respectively. 60

Figure 5. 1 Sheet resistance as a function of the thickness of the graphene films printed on Si/SiO_2 substrate before and after annealing. 70

Figure 5. 2 depicts the sensitivity of the measured thermal phase to changes in various parameters on Al (40nm)/Graphene (225nm)/SiO2/Si structure. 71

Figure 5. 3 Experimental phase data (symbols) with fitted analytical solution (solid lines) for the Al/h-BN/SiO_2/Si structure. 73

Figure 5. 4 In-plane thermal conductivities of printed films as a function of the thickness before (red) and after annealing (black). 75

Figure 5. 5 Monte Carlo histogram for annealed graphene thin film ($K_{\parallel} = 11 \pm 0.56$ W/mK and $k_{\parallel} = 0.33 \pm 0.03$ W/mK). 77

Figure 5. 6 Summarized (a) in plane thermal conductivity, (b) out of plane thermal conductivity, and (c) thermal boundary conductance with Al layer before(circle) and after annealing (rectangle) of graphene (black), h-BN (red), and MoS_2 (navy) films. 79

Figure 5. 7 Calculated thermal conductivity as a function of (a) defect scattering strength Γ for several flake sizes (b) flake size. 83
Figure 5. 8 Minimum out of plane thermal conductivities of graphite (black), h-BN (red), and MoS_2 (blue) as a function of temperature. 84

CHAPTER 1

Introduction and Background

The thermophysical properties of thin film materials play a significant role in a number of technologies, particularly in electronics, optoelectronics, and photonics[1–3]. These devices very often require a high current operation and cause the temperature to rise, which can lead to the degradation of the device performance and reliability. Notably, in nanoelectronic devices, the heat generated travels through several layers and interfaces before reaching a heat sink, and often poor heat conduction in these layers and the resistance at the interfaces become a dominant bottleneck for heat transfer from the active region to the environment. Additionally, in thermoelectric devices, the thermoelectric figure of merit is linearly proportional to the electrical conductivity and inversely proportional to the thermal conductivity which is defined as, $zT = \frac{S^2 \sigma T}{K}$, where S is Seebeck coefficient, σ is the electrical conductivity, T is the temperature, and K is the thermal conductivity. Thus, to get a high thermoelectric figure of merit, a low thermal conductivity value is desirable. So, thermal management in nanoelectronics and higher efficiency in thermoelectric energy conversion have become a concern for continuing progress in the electronics industry and are motivating investigations of thermal transport at the nanoscale[2,3]. Over the last few decades, significant progress has been made to improve the thermoelectric performance by creating nanostructured materials such as superlattices, quantum dots, nanowires, and nanocomposites where the reduction in thermal conductivity is mainly caused by scattering at defects and interfaces[4]. Also, because of the advancement in technology, several experimental techniques have been

implemented to directly characterize the heat transport in bulk materials, thin films, and interfaces[5–9]. However, measuring the thermal properties of anisotropic materials is still challenging because of the difficulty with measuring the in-plane thermal conductivity[10].

In order to optimize heat dissipation problems on devices such as transistors and light-emitting devices based on novel anisotropic materials such as graphene and hexagonal boron nitride (h-BN), it is essential to characterize anisotropic heat conduction as well as boundary conductance of these materials. This requires new or improved measurement techniques. Very recently, printed films made of 2-dimensional materials (2D) based inks have also shown promise due to low-cost device fabrication techniques and potential applications[11–14]. To develop devices that are cognizant of the thermal and electrical properties of these printed films, it is of paramount importance to understand the structure-property relationship, heat and electron transfer mechanisms and to determine how electron and heat transport relate in these materials. This thesis describes the development of techniques to measure anisotropic thermal properties and direct thermal measurements on anisotropic materials and printed films made of 2D materials based inks.

1.1 Thermal Boundary Conductance

The thermal boundary conductance (TBC) is the inverse of the thermal boundary resistance, also known as the Kapitza resistance[15]. TBC resists heat flow at the interface of a boundary between two materials. When a carrier such as an electron or phonon travels through interfaces, it scatters due to different electronic or vibrational properties

of two adjacent materials, which causes resistance to heat transfer at the interface. At room temperature, the highest measured thermal boundary conductance is 14 ± 3 GW/m^{2}K[16] between Palladium (Pd) and Iridium (Ir) and the lowest measured thermal boundary conductance is 8.5 ± 3 MW/m^{2}K[17] between Bismuth (Bi) and Hydrogen-terminated diamond.

Thermal boundary conductance is defined as the ratio of heat flux and temperature gradient at the interface of two materials;

$$G = \frac{J}{\Delta T} \tag{1}$$

The temperature discontinuity is due to the interfacial thermal resistance. In electronic devices, the heat dissipation pathway is from the device to the heat sink end to the ambient environment, and there are several layers and interfaces involved. The resistance at the interfaces can resist efficient heat flow, and so TBC can be the primary heat dissipation bottleneck in these devices. To exemplify, the SiO_2/Si thermal boundary conductance is 28 MW/m^{2}K which is roughly equivalent to the thermal resistance of 52 nm thick SiO_2. Thus poor heat dissipation pathways can lead to the device temperature rise and consequently can degrade the performance and reliability of the device. Therefore, it is essential to transfer heat quickly from the active region to the environment to improve the performance. This means it is urgent to characterize interfaces at the device development stage for better efficiency.

There are two widely used theoretical methods based on phonon transport to predict the interfacial thermal resistance, the acoustic mismatch model and the diffuse mismatch model.

1.1.1 Acoustic Mismatch Model

The AMM model considers a perfect specular interface and the phonons are governed by continuum acoustics[18]. There is a mismatch in acoustic impedance at the interface between dissimilar materials due to the different sound speeds and densities which is analogous to the refractive index mismatch between two materials. For a phonon with normal incidence, the transmission probability from side one to side two is[18]

$$t_{12} = \frac{4Z_1Z_2}{(Z_1 + Z_2)^2} \tag{2}$$

where $Z = \rho c$ is the acoustic impedances, ρ is the mass density, and c is the sound speed.

This means according to the AMM, if the boundary is between two materials with identical acoustic properties, the transmission probability will be 1 and if there is any mismatch, the transmission probability will be decreased. Thus, in the AMM model, since the interface has no interfacial effects, the transmission probability is incorrectly predicted.

1.1.2 Diffuse Mismatch Model

According to the acoustic mismatch model, there is no scattering at the interface. However, in general, high-frequency phonons are scattered from solid surfaces, and the effect of phonon scattering at the interface needs to be considered. Swartz in 1987 proposed the diffusive mismatch model considering the effect of phonon scattering[18]. Diffuse mismatch model considers the interface diffusive which is completely opposite to the specular assumption of AMM model and is accurate for interfaces which are rough compared to the carrier wavelength. This assumption is particularly valid at near room and high temperatures. This model assumes scattering destroys the angular correlation between incoming and outgoing phonons. The scattering probability at the interface is just proportional to the phonon density of states because the acoustic correlations at interfaces are completely destroyed by diffuse scattering. Hence, the transmission probability of the phonon at the interface is just proportional to the mismatch between the phonon density of states[18]. For a phonon, the transmission probability from side one to side two is[19]

$$t_{12} = \frac{\sum_j^3 \int_0^{\omega_{D,j}} \hbar\omega\nu_{2,j}\, D(\omega,\nu_{2,j}) f_{BE} d\omega}{\sum_j^3 \int_0^{\omega_{D,j}} \hbar\omega\nu_{1,j}\, D\left(\omega,\nu_{1,j}\right) f_{BE} d\omega + \sum_j^3 \int_0^{\omega_{D,j}} \hbar\omega\nu_{1,j}\, D(\omega,\nu_{1,j}) f_{BE} d\omega} \qquad (3)$$

where *j* is a particular polarization, ω is the phonon frequency, ω_D is the cutoff frequency, ν is the phonon group velocity, *D* is the density of states, and f_{BE} is the Bose-Einstein distribution.

Compared to the AMM, Diffuse scattering increases the boundary resistance for identical materials and decreases the boundary resistance for different materials[18].

Both DMM and AMM are convenient as they provide reference values for experimental studies. The predicted value sometimes matches with the experimentally measured result and other cases there are discrepancies between theory and experiment as both models do not capture the complexity of the interaction between phonons at real interfaces. Hence the direct measurement of TBC will better characterize the interfaces.

1.2 Techniques for Thermal Measurement

Due to the significance of thermal properties of materials in a wide range of applications, different methods have been implemented to measure the thermal conductivity and heat capacity of bulk materials and thin film materials as well as the TBC. These methods can be classified into steady-state methods and transient methods. In steady-state techniques, the established temperature difference of the material does not change with time, whereas in transient techniques usually the signal is studied as a function of time. Steady-state techniques include absolute technique, comparative technique, radial heat flow method, and steady-state electrical heating methods[20]. In these techniques, the thermal properties are determined by measuring the temperature difference under steady-state heat flow across the sample, and the mathematical data analysis is quite straightforward. These techniques are most suitable to measure the thermal properties of bulk materials. Raman optothermal technique is also in the category of steady-state techniques which was introduced by Balandin and coworkers to measure the thermal

conductivity of single-layer graphene[21]. In this technique, the Raman laser light acts as a heat source to cause a local temperature rise which is measured by employing Raman thermometry[21]. This technique can lead to inaccuracies due to the errors in accurately determining the optical absorption of the sample and heat transfer at the sample boundaries. Transient techniques include pulsed power technique, laser flash method, hot-wire method, 3ω method, time domain thermoreflectance (TDTR) and frequency domain thermoreflectance (FDTR)[20]. The advantage of the 3ω method, TDTR and FDTR is that these techniques can be applied directly to measure the thermal properties of both bulk materials and thin film materials.

The Cahill group first implemented the 3ω method to directly measure the thermal properties of thin films and bulk materials[5]. Although this method can accurately measure the thermal properties of bulk materials and low thermal conductivity dielectric films, the accuracy is limited for highly thermally conductive layers. The main limitation of this method is that modulation frequency is limited at ~100 KHz. This limits the ability to characterize heat transport at shallower depth as the thermal penetration depth l is inversely proportional to the square root of the modulation frequency f ($l = \sqrt{\frac{K}{\pi C f}}$, where C is the volumetric heat capacity and K is the thermal conductivity). Another limitation of this method is that it requires microfabrication for the metallic heater.

With the advancement in technology, optical pump-probe techniques such as transient thermoreflectance and transient absorption have become popular. In the transient thermoreflectance technique, the reflectance is measured which is proportional to the surface temperature rise, whereas in the transient absorption technique, the absorption is measured. The transient thermoreflectance techniques are well recognized

to measure the thermal conductivity, TBC, and volumetric heat capacity of bulk materials and thin films. These techniques are non-contact optical pump-probe methods including TDTR[6,7] and FDTR[8,22,23]. Both methods measure the surface reflectivity with a probe beam, which is related to the surface temperature through the principle of thermoreflectance. TDTR measures the temperature on the surface of a sample as a function of the temporal delay between ultrafast pump and probe pulses, whereas FDTR measures the thermal lag on the surface of a sample with respect to the imposed heat flux from a modulated laser source. A metallic layer (generally referred to as a transducer) is deposited on the surface of the sample whose reflectance changes with surface temperature rise. So, the transducer works both as a thermometer and heater. FDTR does not require the use of ultrafast lasers, electro-optic modulators and long optical delay stages, which makes it cost effective and more straightforward to implement. In both methods, the measured response is used to extract the thermal properties of the sample by fitting it to the solution of the diffusive heat equation[6,7].

1.3 Anisotropy

Anisotropy refers to the direction-dependent property of a material. Depending on the heat flow patterns, materials can be isotropic or anisotropic. Heat conduction in isotropic materials is independent of the spatial orientation around the heat source, whereas the conduction in anisotropic materials varies in different directions. Thermal anisotropy is observed in different types of materials, such as 2D layered materials, polymer materials, many crystals and nanostructured materials.

The intrinsic thermal properties of 2D materials are highly anisotropic. This is mainly because of strong atomic interactions within the basal-plane compared to weak Van der Waals attractions along the cross plane direction. For example, graphite is a highly anisotropic material with an anisotropy of thermal conductivity on the order of 400 between the in-plane and out-of- plane direction[10]. The first experimental studies of the thermal conductivity of suspended graphene exfoliated from high-quality highly oriented pyrolytic graphite (HOPG) performed through optothermal Raman technique revealed *K* around 3000 W/mK near room temperature which is above the bulk graphite limit (~2000 W/mK). The in-plane thermal conductivity of graphene is the highest in any material[24,25]. This high in-plane thermal conductivity is due to strong covalent sp^2 bonding between the carbon atoms and relatively small mass of the carbon atom[26]. Due to the small mass of carbon atoms and strong in-plane sp^2 bonds of graphene, the phonon group velocities of transverse acoustic (TA) phonons and longitudinal acoustic (LA) phonons are very high. The measured longitudinal and transverse phonon group velocities are $\nu_{TA} = 13.6$ Km/s and $\nu_{LA} =$ 21.3 Km/s respectively which lead to the high in-plane thermal conductivity of graphene[27]. Polymer materials can also exhibit strong anisotropic thermal conductivity. The thermal conductivity of polyethylene nanofibers was found ~ 104 W/mK along the chain direction which is due to the restructuring of the polymer chains by stretching which is more than 40 times larger than the transverse direction[28,29]. Isotropic materials also often exhibit anisotropy when processed into thin films due to the nonhomogeneous grains and defects during crystal growth[28]. A variety of other bulk and nanostructured materials also exhibit anisotropy along different lattice directions such as in hexagonal crystals.

Understanding the thermal properties of anisotropic materials is essential for a number of applications. Although over the last few years remarkable progresses have been made, accurately characterizing heat transport remains challenging. Steady-state and laser flash methods can measure the thermal properties in a particular direction by aligning temperature gradient and heat flux on that direction but require big size samples or specific geometry which limits their application[28,30–32]. Modified 3ω technique can also enable anisotropic thermal conductivity measurements but requires complicated micro-fabrications and materials processing[5,28,33]. Compared to these techniques, thermoreflectance techniques such as FDTR and TDTR are mostly used to perform direct measurements on bulk materials and thin films. Typically these techniques are sensitive to out-of-plane conduction. In order to enhance sensitivity to in-plane heat transport, several methods have been introduced, such as varying optical spot sizes which requires realignment of the optics after each measurement[9]. Beam offset approaches can also enhance the sensitivity to in-plane heat transport by probing the surface temperature in the radial direction[7]. Simultaneous measurements of in-plane and out-of-plane thermal conductivities as well as thermal boundary conductance of anisotropic materials can increase measurement accuracy. This requires further enhancement in experimental sensitivity. In this thesis, we have modified FDTR to enhance sensitivity to anisotropic heat conduction which enables direct measurements on emerging anisotropic materials which are promising for device applications.

1.4 Two Dimensional (2D) Materials

2D materials are crystalline layered materials and often only one atom thick. The 2D materials family includes the most promising graphene, hexagonal boron nitride (h-BN), black phosphorous (BP), and transition metal dichalcogenides such as Molybdenum disulfide (MoS_2), Molybdenum diselenide ($MoSe_2$), and Tungsten disulfide (WS_2).

Among the above 2D materials, graphene is superior due to its excellent thermal properties, fast electron mobility, and highest mechanical strength, and is also commonly used in Van der Waals heterostructures[34]. These exceptional properties make graphene attractive for a broad range of applications in electronics and optoelectronics devices, circuits, photonics to biosensors and solar cells[11,34–37]. Hexagonal boron nitride (h-BN), also referred to as white graphene, has a similar structure and high thermal conductivity but it is an electrical insulator. h-BN is very convenient as a dielectric and tunnel barrier, as it can be readily integrated with other 2D materials to create heterostructures[35]. As a substrate for graphene devices, h-BN significantly enhances the charge carrier mobility and thermal conductivity of graphene which are desirable for high-performance graphene devices[35,38,39]. At room temperature, the thermal conductivity of h-BN supported graphene is calculated to be 1,345 W/mK, about twice that of SiO_2-supported graphene[39].

Semiconducting layered materials based on transitional metal dichalcogenides (TMDs) such as MoS_2, WS_2, and $MoSe_2$ have also shown attractive qualities for applications in electronic, optoelectronic, and spintronic devices[40–46]. MoS_2 is particularly attractive in photonics and optoelectronics given the large on-off current ratios in devices and layer-dependent bandgap, which is direct for single-layer MoS_2, indirect otherwise[40–

[42]. Monolayer MoS_2 exhibits stronger photoluminescence compared to other TMDs. However, $MoSe_2$ has a higher electrical conductivity as well as a direct bandgap, which is beneficial to applications such as transistors and photodetectors[43–45]. WS_2 has a direct band gap of ~2.1 eV with high in-plane mobilities which make it promising for light-emitting diodes and optical sensors[46].

In this thesis, we employ frequency domain thermoreflectance incorporating different techniques such as beam offset and Kerr effect to measure anisotropic thermal conductivity and TBC simultaneously to a range of 2-dimensional materials with enhanced sensitivity which are of interest for novel device applications, including single-layer graphene, MoS_2, few-layer h-BN, and MoS_2, and single crystal WS_2 and single crystal $MoSe_2$.

1.5 Solution Processed (2D) Materials

The research on ink systems of graphene and related 2D materials including TMDs and h-BN which can be exfoliated from their parent materials via solution processing, promises the same intensity of research as these 2D materials, due to the compatibility with flexible substrates, low-cost fabrication, and mass production methods. Consequently, these ink systems attract potential interest in various applications, particularly in sensors, electronics, optoelectronic devices, and printing technologies[11–13,24,25,47,48]. In particular, printed films of such inks could have possible use in thermal, and in particular, in thermoelectric applications, where improvement in electrical conductivity but not thermal conductivity is required for a higher thermoelectric figure of merit.

Solution-processed 2D materials can also provide great flexibility in the creation of complex heterostructures by combining different layers which allow controlling the electronic, optical and mechanical properties of the resulting materials and can enable novel applications. Graphene is also particularly attractive as a nanofiller in composites, as it enhances the thermal and electrical properties of the matrix materials due to its excellent conduction properties. Solution-processed graphene can be produced easily and can be used as a filler on a mass scale.

Although several investigations have been done to measure the electrical properties of 2D-materials based inks, very little is known about their thermal properties. In this thesis, we measure the electrical conductivity and in-plane and out-of-plane thermal conductivities of graphene and other 2D-materials thin films produced by ink-jet printing of water-based 2D-materials inks[13].

1.6 Organization of the Thesis

This thesis consists of 6 chapters. The first chapter provides a basic introduction about thermal boundary conductance, different thermal measurement techniques, thermal anisotropy, 2D materials, solution-processed 2D materials and their applications. Chapter 2 starts with the description of frequency domain thermoreflectance (FDTR) in detail including all the optics used to carry out the measurements, spot size measurement, numerical modeling, sensitivity analysis, and Monte Carlo computational method for uncertainty calculation. Chapter 3 illustrates the development of beam offset frequency domain thermoreflectance (BO-FDTR) used to enhance the sensitivity to in-

plane thermal transport and thermal measurements on several anisotropic materials. Then in chapter 4, I describe the implementation of frequency domain magneto-optical Kerr effect (FD-MOKE) which allows us to use a thin magnetic transducer and further enhances the sensitivity to lateral heat transport. We measure the anisotropic thermal conductivity of a range of 2D materials as well as TBC by taking advantage of both beam offset and MOKE. Chapter 5 presents the thermal conductivity measurements on printed films made of graphene, h-BN, and MoS_2 based inks. We also observe the effect of annealing, thickness dependency on thermal properties of these printed films. Chapter 6 summarizes the work and provides future direction for thermal studies, particularly for anisotropic materials.

CHAPTER 2

Frequency Domain Thermoreflectance (FDTR)

2.1 Overview

Frequency domain thermoreflectance (FDTR) is an optical pump-probe technique used to measure the volumetric heat capacity, in-plane and out-of-plane thermal conductivity, and thermal boundary conductance of bulk materials and thin films, and it has several advantages over time domain thermoreflectance (TDTR). FDTR requires a very smooth surface so that light can be reflected back to the detector without distortion. So far, FDTR has been successfully used to measure the thermal properties ranging from very highly thermally conductive materials like graphite and graphene, to low conductivity amorphous materials like glass. This chapter provides a brief introduction on FDTR, including experimental setup and numerical modeling, comparison with TDTR, spot size measurements, and robust uncertainty calculations for fitted values.

2.2 Difference Between TDTR and FDTR

FDTR and TDTR are optical pump-probe transient thermoreflectance techniques where changes in the reflectance, which are proportional to the surface temperature rise are measured after the absorption of a pump laser. The change in temperature due to the pump pulse effects the refractive index of the sample, and hence the reflectivity also

changes. The relation between the relative change in reflectivity and the temperature change can be approximated to first order as[49],

$$\frac{\Delta R}{R} = \left(\frac{1}{R}\frac{\partial R}{\partial T}\right)\Delta T = C_{TR}\Delta T \quad (4)$$

where C_{TR} is the thermoreflectance coefficient (which depends on the sample, wavelength of the illuminating light, and the angle of incidence), *R* is the illuminated intensity reflected from the surface of the sample, and *T* is the surface temperature. Both methods are well recognized for the accuracy of their thermal measurement. The fundamental difference between both techniques is that TDTR measures the temperature on the surface of a sample as a function of the time delay between ultrafast pump and probe lasers, whereas FDTR measures the phase lag between the incident heat flux and the surface temperature rise. The main advantage of FDTR over TDTR is that FDTR does not require ultrafast lasers, long mechanical delay stages and electro-optic modulators, and thus making it straightforward to implement. Additionally, while in TDTR the range of modulation frequency is limited, in FDTR the signal can be detected over a wide range of frequencies, enhancing the sensitivities to several parameters of interest, allowing the simultaneous determination. In both methods, the measured response is used to extract the thermal properties of the sample by fitting it to the solution of the diffusive heat equation.

2.3 Analytical Modelling

The diffusive heat transport modeling framework used to determine the thermophysical properties of single and layered materials from thermoreflectance measurements is well established[6,7,9]. When the surface of a semi-infinite solid is heated by a periodic point source of unit power at angular frequency ω, the frequency domain solution is[6]

$$g(r) = \frac{exp^{(-qr)}}{-2\pi Kr} \tag{5}$$

and

$$q^2 = (\frac{i\omega}{D}) \tag{6}$$

where K is the thermal conductivity, D is the thermal diffusivity, q is the heat flux, r is the radial coordinate, and *g(r)* is radially symmetric.

The solution for the infinite solid is a factor of 2 that of a semi-infinite solid. The co-aligned laser beams of TDTR or FDTR experiment have cylindrical symmetry. Hankel transforms are used to simplify the convolution of this solution with the distribution of laser intensities. The Hankel transform is equivalent to a two dimensional Fourier transform with a radially symmetric integral Kernel, and also referred to the Fourier Bessel transform. The Hankel transform of $g(r)$ is[6]

$$G(h) = 2\pi \int_0^\infty g(r)\, J_0(2\pi hr) r dr \tag{7}$$

$$G(h) = \frac{1}{K(4\pi^2 h^2 + q^2)^{1/2}} \tag{8}$$

where J_0 is the zeroth order Bessel function of the first kind, and h is the Hankel transform variable.

The pump beam used in a typical FDTR or TDTR experiment to heat the surface of the sample has a Gaussian intensity distribution $p(r)$, which is[6]

$$p(r) = \frac{2A_p}{\pi {w_0}^2} exp(-\frac{2r^2}{{w_0}^2}) \tag{9}$$

where w_0 is the $\frac{1}{e^2}$ radius of the pump laser beam and A_p is the amplitude of the heat absorbed by the sample at frequency ω.

The Hankel transform of $p(r)$ is[6]

$$P(h) = Aexp(-\frac{\pi^2 h^2 {w_0}^2}{2}) \tag{10}$$

The inverse transform of the product of $G(h)$ and $P(h)$ is the distribution of the temperature oscillations at the surface of the sample $\theta(r)$, which is[6]

$$\theta(r) = 2\pi \int_0^\infty P(h)\, G(h)\, J_0(2\pi hr) h dh \tag{11}$$

In the thermoreflectance technique, the change in reflectivity is measured by changes in the intensity of a reflected probe laser beam which is proportional to the surface temperature rise. The probe beam used in a typical FDTR or TDTR experiment also has a Gaussian intensity distribution with same or different $\frac{1}{e^2}$ radius. The probe beam measures the weighted average of the temperature distribution $\theta(r)$, which is[6]

$$\Delta T = \frac{4}{{w_1}^2} \int_0^\infty \theta(r) \exp\left(-\frac{2r^2}{{w_1}^2}\right) r dr \tag{12}$$

where the $\frac{1}{e^2}$ radius of the probe laser beam is w_1.

This integral over *r* is the Hankel transform of a Gaussian which leaves a single integral over *h*[6]

$$\Delta T = 2\pi A \int_0^\infty G(h)\, exp\left(-\frac{\pi^2 h^2 (\, {w_0}^2 + \, {w_1}^2}{2}\right) h dh \tag{13}$$

The upper limit of the integral can be set to $\left(\frac{2}{(\, {w_0}^2 + {w_1}^2)^{1/2}}\right)$. This equation is unchanged by an exchange of the radius of the pump or probe beam[6].

For a layered geometry, $G(h)$ of equation (13) can be obtained through an iterative procedure developed by Feldman[50], numbering the layers starting from the transducer layer at $n = 1$. Practically, heat cannot reach the other side of this bottom layer at rates comparable to the modulation frequency and therefore, $B^+ = 0$ and $B^- = 1$ for the final/bottom layer[6].

$$\begin{pmatrix} B^+ \\ B^- \end{pmatrix}_n = \frac{1}{2\gamma_n} \begin{pmatrix} \exp(-u_n L_n) & 0 \\ 0 & \exp(-u_n L_n) \end{pmatrix} \times \begin{pmatrix} \gamma_n + \gamma_{n+1} & \gamma_n - \gamma_{n+1} \\ \gamma_n - \gamma_{n+1} & \gamma_n + \gamma_{n+1} \end{pmatrix} \begin{pmatrix} B^+ \\ B^- \end{pmatrix}_{n+1} \tag{14}$$

$$\gamma_n = K_n \mathrm{u}_n \tag{15}$$

$$\mathrm{u}_n = (4\pi^2 h^2 + q_n^2)^{1/2} \tag{16}$$

$$q_n^2 = \frac{i\omega}{D_n} = \frac{i2\pi f}{D_n} \tag{17}$$

Each layer *n* is described by three parameters; the thermal conductivity K_n, thermal diffusivity D_n, and thickness L_n.

Thus for a layered structure, $G(h)$ in equation (13) is replaced by[6]

$$G(h) = \left(\frac{B_1^+ + B_1^-}{B_1^- - B_1^+}\right)\frac{1}{\gamma_1} \tag{18}$$

For the anisotropic case, γ_n and u_n are defined as[7],

$$\gamma_n = K_{\perp,n}\mathrm{u}_n \tag{19}$$

$$\mathrm{u}_n = (4\pi^2 h^2 \frac{K_{\parallel,n}}{K_{\perp,n}} + q_n^2)^{1/2} \tag{20}$$

where, $K_{\perp,n}$ and $K_{\parallel,n}$ are cross-plane and in-plane thermal conductivities respectively. Thermal boundaries are modeled as layers having $L = 1$ nm, negligible heat capacity, and equivalent $K_e = HL$, where H is the boundary conductance[6].

2.4 Sensitivity

The sensitivity of the measured phase signal θ (the phase of the complex temperature in eq. (13)) due to a change in parameter x is defined as

$$S = \frac{d\,\theta}{d\ln x} \tag{21}$$

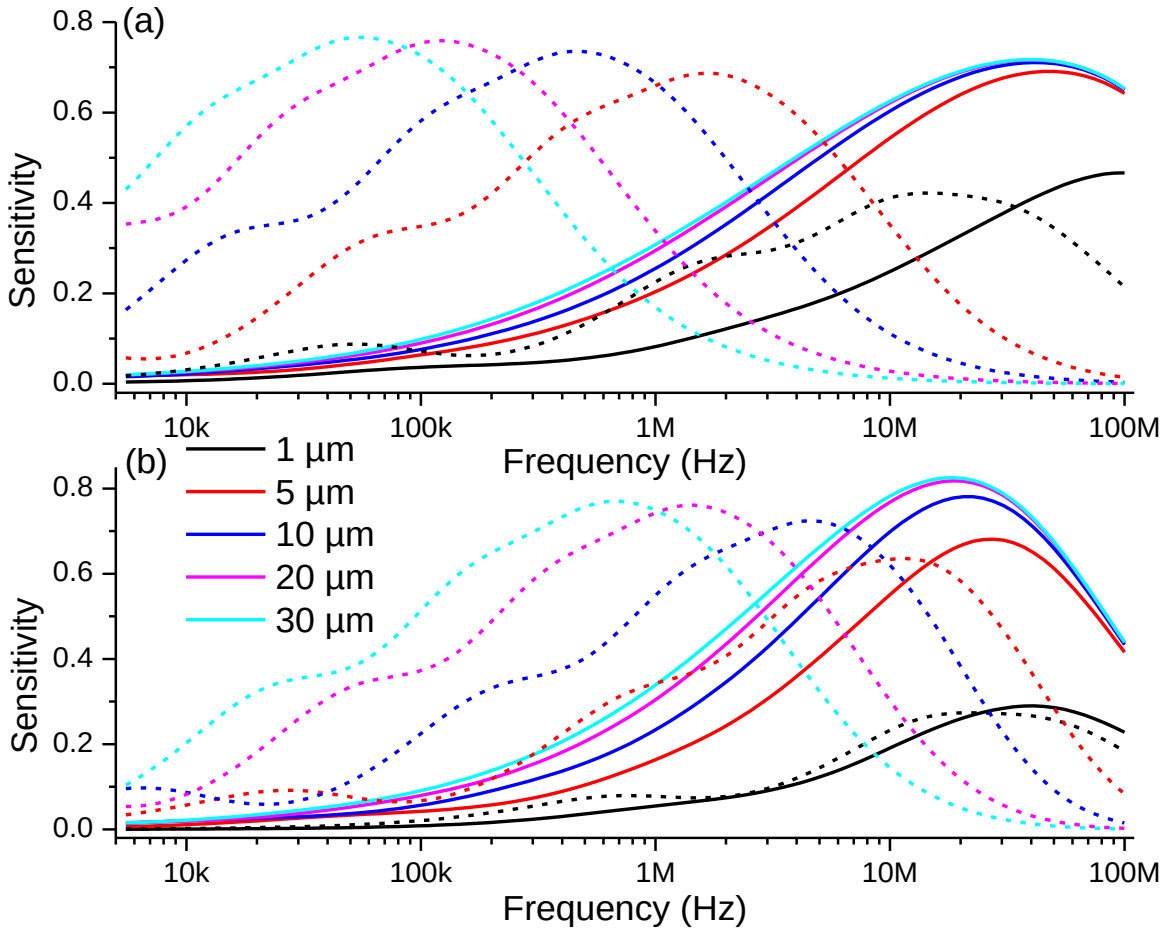

Figure 2. 1 depicts the sensitivity to $K_{\parallel}$, (dash lines) and $K_{\perp}$ (solid lines) of (a) Si for the Al (50nm) / Si structure and (b) graphite for the Al (50nm) / graphite structure for several RMS spot sizes.

The sensitivity to measurements to the parameters of interest, such as $K_{\perp}$, $K_{\parallel}$, and TBC depends in a complex way on the thermophysical properties of the layers comprising the sample, and insight on which property can be determined through measurement can be obtained by analysis of the measurement sensitivity as described below. For the case of a high thermal diffusivity thin film (transducer) on a thermally isotropic bulk medium, sensitivity to measuring $K_{\perp}$ is enhanced at larger spot sizes and higher modulation frequencies (small thermal penetration depth), given the 1D out-of-plane isotherms

obtained in this regime[51,52]. The thermal penetration depth is defined as the depth normal to the surface at which the amplitude of the temperature is $\frac{1}{e}$ of its surface temperature. On the other hand, when in-plane thermal diffusion length is comparable or larger than the laser spot size, the isotherms are more spherical, and heat transport is more 3D, allowing for the determination of $K_{\parallel}$. This can be achieved at large spot sizes and low modulation frequencies or at high frequencies and small spot sizes. The sensitivity to in-plane and out-of-plane thermal conductivities of Si for the Al (50nm)/Si structure and of graphite for the Al (50nm)/graphite structure for several RMS spot sizes is shown in Figure 2.1. The sensitivity to in-plane transport will be further enhanced when the thermal diffusivity of the substrate is much smaller than that of the thin film, leading to 2D in-plane transport.

2.5 Experimental System

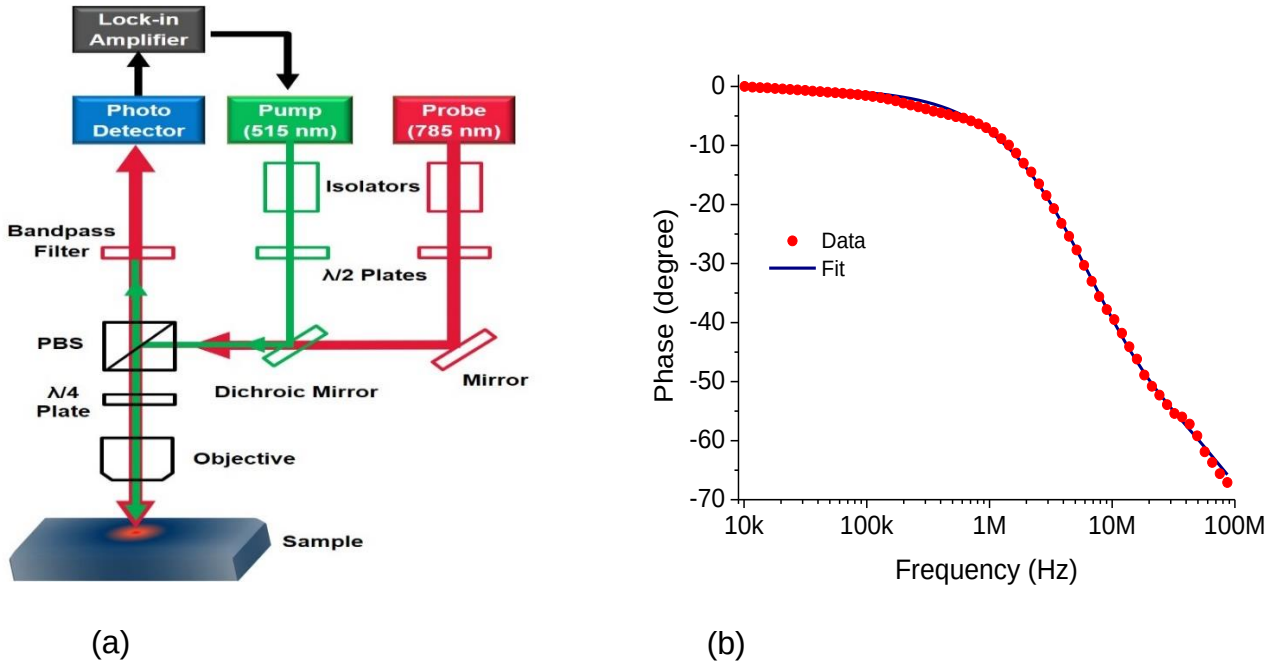

(a) (b)

Figure 2. 2 (a) FDTR Setup. (b) Experimental phase data with analytical fit on Al/SiO_2/Si sample structure with modulation up to ~100 MHz.

The schematic diagram of our FDTR experimental setup is shown in Figure 2.2(a). The experimental setup of our FDTR is based on two CW Omicron A350 lasers operating at 515 nm (pump) and 785 nm (probe). A metallic layer is typically deposited on the surface of the sample which acts as both thermometer and heater and is referred to as a transducer. We generally use Al transducers due to the high coefficient of thermoreflectance at the probe wavelength (785 nm). The pump laser is directly modulated through its analog input using a Lock-in Amplifier (Zurich instruments HF2LI) and focused onto the surface of the sample using a 40X objective (Olympus RMS40X),

whereas the probe beam remains unmodulated. The 40X objective reduces the RMS laser spot size to ~1.4 microns, which increases the thermoreflectance signal due to the increase in surface temperature oscillations and thus allows detecting signal over a wide range of frequencies. Both beams pass through optical isolators (Con-Optics M711A and M712B) to prevent back reflections into the lasers which can destabilize the laser sources. A polarizing beam splitter (PBS) (Thorlabs PBS 251) is used to allow vertically polarized pump and probe beams toward the sample which are polarized circularly when passing through the quarter wave plate (QWP) and focused onto the sample surface. When the reflected pump and probe beams travel back through the QWP, the circularly polarized light is reversed into horizontally polarized light, and the PBS redirects both beams toward the photodetector (Thorlabs PDA8A).

After the absorption of the modulated pump beam, the periodic heat flux causes the surface temperature to change periodically at that frequency, but with an additional thermal phase lag $\theta_{thermal}$. Two measurements are required to extract the desired thermal phase from additional instrumental contributions that make up the total measured phase. We refer to the first measurement as the thermal measurement (θ_1), performed by detecting the probe beam, and the second as the reference measurement (θ_2), performed by detecting the pump. Two optical band pass filters (515 nm and 785 nm band pass filters) are used to separate the pump and probe beams before the photodetector. The contributions to the two FDTR measurements are: $\theta_1 = \theta_{thermal} + \theta_{optical} + \theta_{electrical} + \theta_{reference}$ and $\theta_2 = \theta_{optical} + \theta_{electrical} + \theta_{reference}$. Therefore, $\theta_{thermal} = \theta_1 - \theta_2$, since both signals travel through the same optical and electrical paths. The measured thermal phase$\theta_{thermal}$ is then fitted to the diffusive heat equation to extract

the thermal phase of interest. The measured phase data through our FDTR system together with the fitted analytical solution for the Al/SiO_2/Si sample structure is shown in Figure 2.2 (b). A very small RMS laser spot size allows us to modulate up to ~100 MHz. When the carrier's mean free path is comparable with or exceeds pump spot size or thermal penetration depth $l = \sqrt{\frac{K}{\pi C f}}$, non-diffusive heat transport phenomena may occur[53,54], where *C* is the volumetric heat capacity, K is the thermal conductivity and *f* is the modulation frequency. Since we use a small RMS spot size, modulating at such high frequencies can lead us to study non-diffusive heat transport.

2.6 Spot Size Measurement

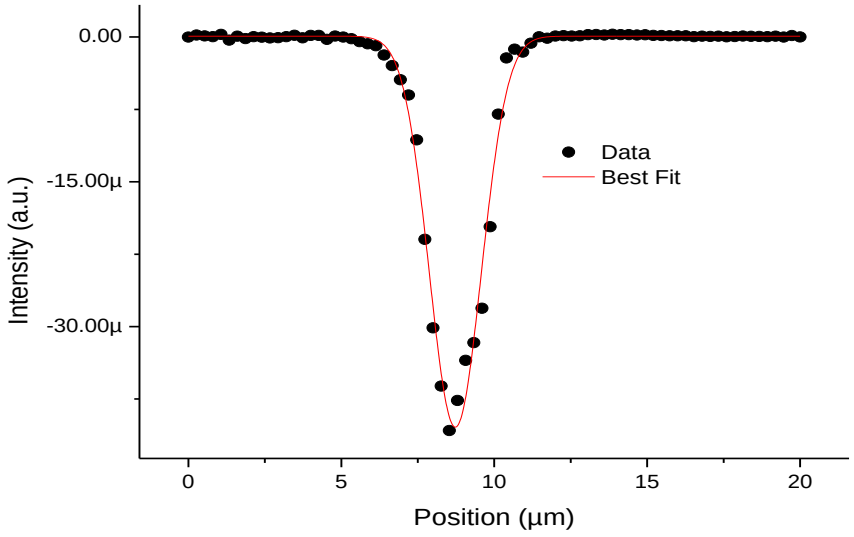

Figure 2. 3 Pump spot size measurement

Since we work with small spot sizes, the accurate determination of spot size is critical to reduce sources of experimental error. The spot sizes of the pump and probe beams are

measured using a knife-edge technique. In our FDTR measurements, we use a small RMS spot size to obtain a large thermoreflectance signal. We measure the pump and probe spot sizes when the RMS spot size is smallest and thus we first maximize the thermal signal. Then the reflected pump and probe signal is measured separately as a function of the translation stage. A power meter records the total power of the beam at each location. The derivative of the recorded power yields the intensity profile along the x-direction which is then fit into a Gaussian profile to extract the $\frac{1}{e^2}$ radius of the beam. A schematic fit for the green spot is shown in Figure 2.3. The RMS spot size is then calculated using the following equation;

$$r_{RMS} = \sqrt{({r_{pump}}^2 + {r_{probe}}^2)/2} \tag{22}$$

The measured RMS spot size is ~1.4 μm.

2.7 Monte Carlo Computational Method for Uncertainty Calculation

A Monte Carlo computational approach is used to calculate the measurement uncertainty due to the uncertainties of the input parameters in the diffusive heat model[55]. The input parameters are considered to have a normal distribution about their mean value with a standard deviation which is estimated from several independent measurements.

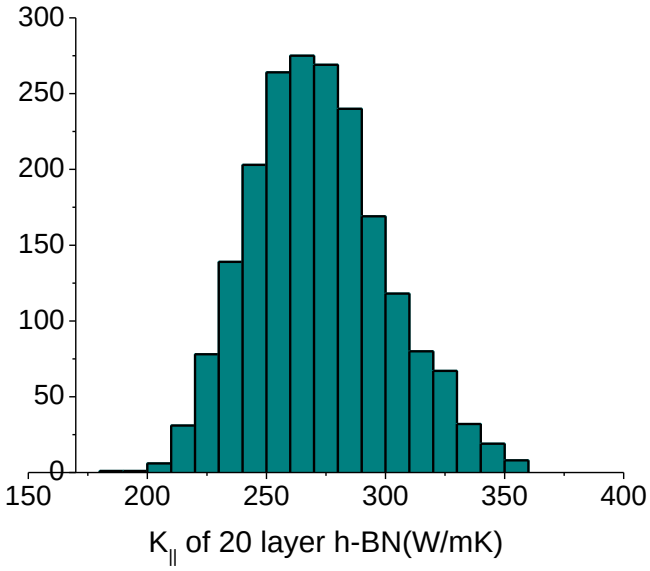

Figure 2. 4 Histogram from Monte Carlo simulation. The resulting value for $K_{\|}$ is 270 ± 28.2 W/mK.

The uncertainty in phase from experimental noise contribution is also included. In each Monte Carlo simulation run, a new set of nominal input parameters and noisy experimental data are selected randomly. Then using these input parameters, the experimental data are fitted to the diffusive heat equation to extract the fitting parameters that minimize the error between the model and experiment. We repeat the procedure 2000 times until the outcomes reach a normal distribution. For each Monte Carlo run both the fitted parameters and goodness of fit are recorded, the latter is used to weigh the value of its associated parameter for statistical significance. Finally, we calculate the weighted average and standard deviation of the fitted parameters of interest. For example, the fitted values for in-plane thermal conductivity of h-BN are K_1, K_2, …. K_N and the uncertainties from the goodness of fit are σ_1, σ_2 , … σ_N. The weighted average

is then calculated as

$$K_{avg} = \frac{\sum_{i=1}^{N} W_i K_i}{\sum_{i=1}^{N} W_i} \quad (23)$$

where weight $W_i = \frac{1}{\sigma_i^2}$.

The resulting histogram of in-plane thermal conductivity of few-layer h-BN is shown in Figure 2.4.

2.8 Summary

Our FDTR is very useful to measure the thermal conductivity, thermal boundary conductance, and volumetric heat capacity of thin films and bulk materials. We can modulate up to ~100 MHz which can help us to study non-diffusive heat transport without the need for complicated techniques like heterodyne measurement technqiues[22]. Using our FDTR the thermal properties can be measured over a broad range of thermal conductivity values and the measured thermal properties will be beneficial for novel device applications.

CHAPTER 3

Thermal Transport in Anisotropic Materials Through Beam Offset FDTR[1]

3.1 Overview

2D layered materials are very attractive for device applications due to their unique combination of electrical, thermal and optical properties, and the great flexibility they provide in the creation of complex heterostructures[11,34–36,56]. Their intrinsic thermal properties are highly anisotropic and are still being investigated[24,57,58]. In spite of the high thermal conductivity commonly observed along the basal plane of 2D materials, out-of-plane thermal transport across a metallic contact or an insulating support is typically poor[9,47,59–62] leading to heat dissipation bottlenecks in electronic devices. Hence the investigation of heat transport in device-like structures is especially important.

The determination of the in-plane thermal conductivity of some anisotropic materials has been demonstrated using TDTR[9] and FDTR[47]. However, in order to increase the sensitivity to in-plane heat transport, the spot size of the beams needs to be varied[9], which requires the realignment of the optics. This can be a tedious task in systematic studies, and the accuracy obtained when performing a global fit to a spot size-dependent data set, which is necessary to obtain self-consistent results, is reduced by the overall experimental error. Alternatively, collecting data over a wide range of modulation frequencies also improves the sensitivities to in-plane transport, as this

[1] This chapter has been published on Journal of Applied Physics 123, 245110 (2018) with contributions from co-authors M. Shahzadeh, P. Braeuninger-Weimer, S. Hofmann, O. Hellwig, and S. Pisana.

becomes important at relatively high frequencies (~10 MHz). Beam-offset approaches, where the pump and probe beams are no longer coaxial, also increase the sensitivity to in-plane heat transport by directly sampling the surface temperature of the sample in the radial direction[7]. To obtain a more complete picture of the heat transport, the in-plane and out-of-plane thermal conductivities as well as TBC of these materials should be measured. Therefore, combining different approaches that increase the sensitivities to the various parameters of interest, as well as enriching the data sets by increasing the number of independent measurements, can provide a sufficiently complete data set to extract these unknowns simultaneously. Despite the importance of in-plane heat transport in 2D materials, there are only a few reports that demonstrate the determination of anisotropic thermal conductivity using FDTR[8,23,47,63]. These rely on either working with small spot sizes[8,10,29] or on beam offsetting[42]. However, if the experimental parameters are not associated with sufficiently high sensitivities, or the measurements do not span a sufficiently wide parametric range, the results can be plagued with relatively large error bars[42].

Here, we present a beam-offset FDTR (BO-FDTR) approach in which we combine the schemes outlined above in order to measure the thermal conductivity anisotropy and TBC from a single data set obtained at multiple beam offsets. We employ small spot sizes and modulate the pump beam over a wide range of frequencies up to 50 MHz. At high frequencies the signal to noise ratio is typically very low due to the thermal response of the sample (proportional to $f^{-1/2}$, where f is the modulation frequency), and the presence of coherent RF noise. The maximum reported modulation frequency in FDTR is 50 MHz for a coaxial geometry[29], though the use of heterodyne measurement techniques have

extended detection frequencies to 200 MHz[22,64]. In BO-FDTR, the maximum reported modulation frequency is only 6 MHz because the signal strength further decays when the probe beam samples only a portion of the thermal footprint given by the pump beam[42]. Here, we use spot sizes of about 1.4 μm, which yield high enough signals to allow measurements up to 50MHz at large beam offset values without the need of heterodyne measurement techniques. The coherent RF noise at high modulation frequencies can be reduced when necessary by taking reference noise measurements concurrently and subtracting the noise from the thermal signal, avoiding more complicated techniques such as heterodyning[9,43]. This approach allows us to reach large offsets above 1.4ω (where ω is the root-mean-square (RMS) beam radius at $1/e^2$).

3.2 Sample Preparation

Graphene was synthesized by chemical vapor deposition (CVD) using Cu as catalyst and the subsequent transfer to SiO_2/Si substrates was performed using PMMA (poly(methyl methacrylate)) as a support and $FeCl_3$ chemical etching to remove the Cu[65]. Sapphire crystals (Crystech) were annealed in an oxidizing atmosphere before transducer deposition. A clean surface of highly-ordered pyrolytic Graphite crystals (SPI Supplies) was obtained by exfoliating the top layers with adhesive tape before transducer deposition. Al transducers were deposited by thermal evaporation or sputter deposition. White light interferometry or X-ray reflectivity was used to determine layer thickness, and 4-point probe electrical measurements for thermal conductivity via the Wiedemann-Franz law, respectively. The Al transducers for the Graphene and Graphite samples were 52

and 59 nm thick, respectively, and had thermal conductivities of 35.5 W/mK and 33 W/mK, respectively. This value may have been affected by small grain sizes and the presence of residual oxygen in the deposition chamber. The Al transducers for the Sapphire samples were 55 nm thick and had a thermal conductivity of 170 W/mK .

3.3 Theory and Sensitivity Analysis

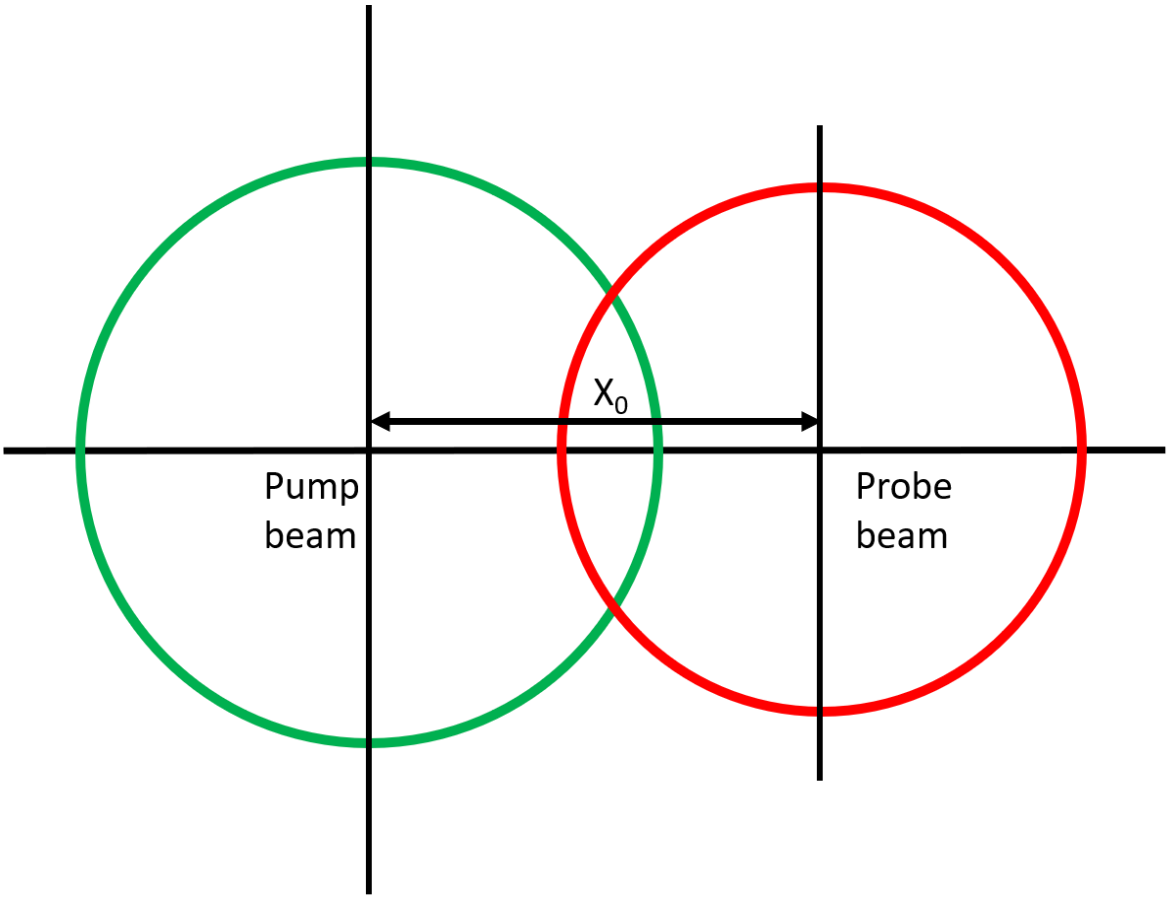

Figure 3. 1 The probe beam is focused at an offset X_0.

The temperature fluctuation detected by the probe beam which is given by equation (13) can be written as,

$$\Delta T = \frac{2\pi}{A_s}\int_0^\infty G(f,h)P(h)S(h)hdh. \tag{24}$$

where $P(h)$ and $S(h)$ are the Hankel transforms of the intensity profiles of the Gaussian pump and probe beams, A_s is the total intensity of the sensing beam, and $G(f,h)$ is the Hankel transform of the frequency domain solution of the heat equation in multilayered media, with h being the Hankel transform variable.

In the case of sensing with an offset probe beam, $S(h)$ of equation (24) is defined as[7]

$$S(h) = \frac{A_s}{\pi}\exp\left\{-\left[\left(\frac{\sqrt{2}x_0}{\omega_s}\right)^2 + \left(\frac{\pi\omega_s h}{\sqrt{2}}\right)^2\right]\right\}\sum_{n=0}^{\infty}\frac{1}{(n!)^2}\left(\frac{\sqrt{2}x_0}{\omega_s}\right)^{2n} l_n\left(\frac{\omega_s h}{\sqrt{2}}\right) \tag{25}$$

where, x_0 is the offset between pump and probe beams as shown in the Figure 3.1, ω_s is the probe spot size and $l_n(x)$ is defined recursively as

$$l_{n+1}(x) = -\frac{1}{x}\left[(\pi^2x^3 - x)l_n(x) + \left(\frac{1}{4\pi^2} - x^2\right)l_n'(x) + \frac{x}{4\pi^2}l_n''(x)\right] \tag{26}$$

where $l_n'(x)$ and $l_n''(x)$ are the first and second derivative, respectively of $l_n(x)$, and $l_0 = \pi$.

We note that this model considers only diffusive heat transport. Small spot sizes and high modulation frequencies can lead to non-diffusive (quasi-ballistic) heat transport. Non-diffusive heat transport can take place when the heat carrier's mean free path becomes comparable with, or exceeds, the pump spot size or the diffusive heat penetration depth $\ell = \sqrt{K/\pi Cf}$[53,66]. Predicting when a departure from diffusive transport occurs can be complicated, as non-diffusive transport may take place anisotropically[53], according to heater geometry[66], or depend on the nature of the interface between two

materials[54]. Analysis of experimental data in which non-diffusive transport takes place using a model that only considers diffusive heat transport often leads to obtaining thermal conductivities that fall below that of bulk values or frequency-dependent thermal properties. Therefore, care must be taken in interpreting the results of experiments when non-diffusive transport may take place.

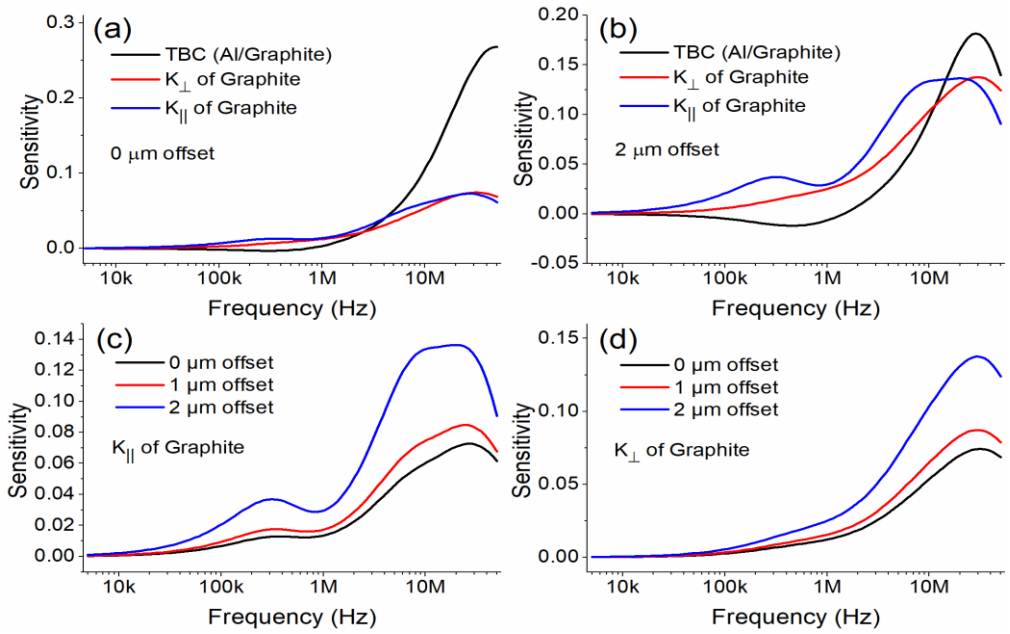

Figure 3. 2 (a) and (b) depict the sensitivity of the measured thermal phase to changes in various parameters at 0 μm and 2 μm beam offsets respectively, (c) and (d) show the sensitivities to in-plane thermal conductivity and out-of-plane thermal conductivity of Graphite, respectively, for several values of beam offsets.

The sensitivity to in-plane transport can be further enhanced when the thermal diffusivity of the substrate is much smaller than that of the thin film, leading to 2D in-plane transport. In most cases, sampling the in-plane transport will be enhanced when the pump and probe beams are offset.

We considered at first a simple Al/graphite system for sensitivity analysis as shown in Figure 3.2 using the input values from Table 3.1. The sensitivity of the measured thermal phase signal due to various thermal parameters of a nominal Al/graphite sample is shown in Figures 3.2(a) and 3.2(b), for the concentric and 2 μm beam-offset cases, respectively, using an RMS spot size of 1.4 μm. By comparing the sensitivities at different offset values, we can determine that there is a high sensitivity to the anisotropic thermal conductivity of graphite over a wide range of frequencies, as well as the TBC of Al/graphite. These three parameters are distinguishable due to their dissimilar spectral sensitivity as the beam offset is varied. The sensitivity to $K_{\parallel}$ is enhanced at lower frequencies with respect to $K_{\perp}$ when the beams are offset, since the heat will diffuse with a longer thermal penetration depth in the radial direction where the probe beam can detect it. This is a common feature of BO-FDTR sensitivity curves. Without beam-offsetting, lateral heat spreading would only be sampled by the periphery of the probe beam, where the light intensity is low and the detected thermal phase changes by a small amount. Figures 3.2 (c) and (d) show the sensitivities of the thermal phase signal to the in-plane thermal conductivity and out-of-plane thermal conductivity of Graphite, respectively, as the beam offset is varied from 0 to 2 μm. As shown, larger beam offsets comparable to the spot size are desirable to significantly increase the sensitivities to the in-plane transport.

*Table 3. 1 Nominal values for fitting and sensitivity analysis. Thickness values are obtained by white light interferometry or X-Ray reflectivity. The K for Al is assumed isotropic and determined by four point probe. *: the value of K for Al for these samples may have been affected by small grain sizes and the presence of residual oxygen in the deposition chamber. Blank values indicate a property that was obtained from fits to the experimental data.*

Property	**Graphite Sample**	**Graphene Sample**	**Sapphire Samples**
Thickness of Al (nm)	59	52	55
C_v of Al (MJ/m^{3}K)	2.42[67]	2.42[67]	2.42[68]
$K_\perp$ of Al (W/mK)	33*	35.5*	170
$K_\parallel$ of Al (W/mK)	33*	35.5*	170
C_v of Substrate (MJ/m^{3}K)	1.6[68]	SiO_2=1.59[69], Si=1.64[70]	3.03[71]
$K_\perp$ of Substrate (W/mK)	5.7[9]	SiO_2=1.32[5], Si=145[72]	-
$K_\parallel$ Substrate (W/mK)	1950[19]	SiO_2=1.32[5], Si=145[72]	-
TBC of Al/Substrate (MW/m^{2}K)	50[59]	-	-

3.4 Experimental Method for Beam-offset FDTR

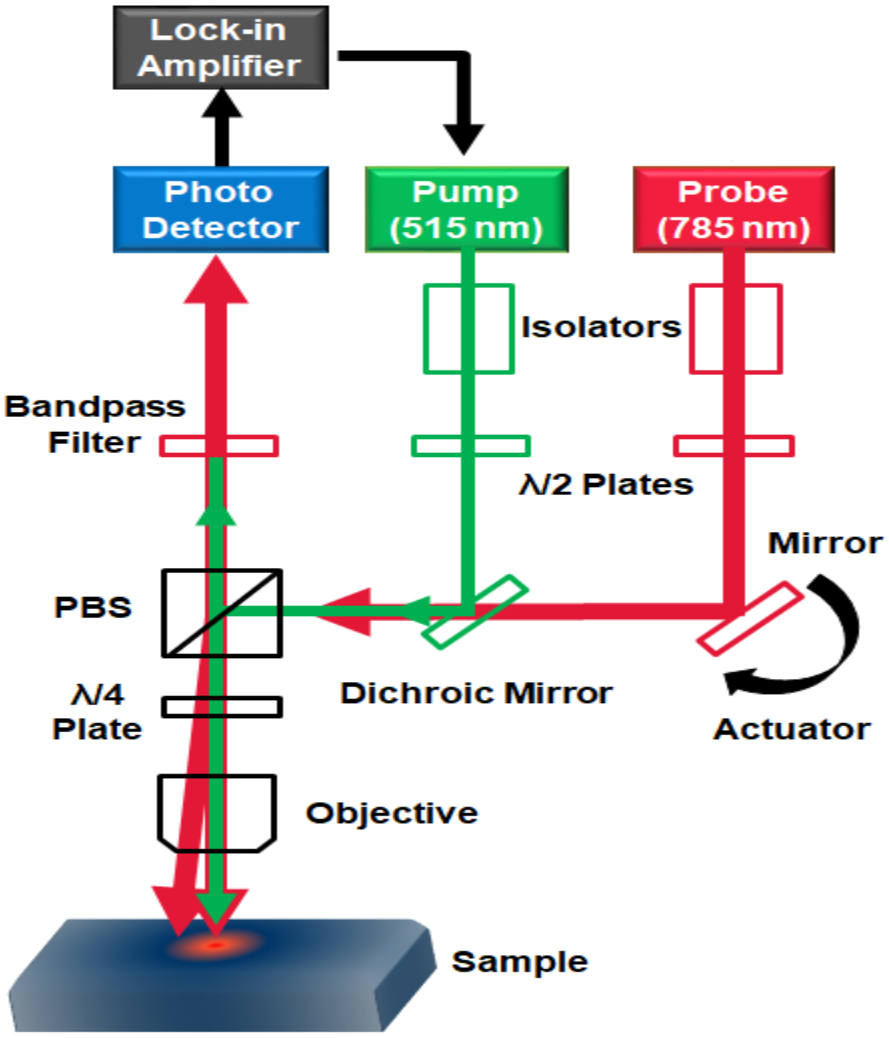

Figure 3. 3 Schematic diagram of beam-offset FDTR

The experimental setup of BO-FDTR is shown in Figure 3.3. The setup is similar to the FDTR setup except the installment of an actuator (Newport TRA12CC Actuator). To offset

the probe beam, we use this actuator to steer a mirror. Care must be taken to ensure that the reflected probe beam is not cropped by optical elements in the sample-to-detector trajectory, and that it remains centered on the photodetector. Proper optical alignment and a focusing lens before the detector mitigate these issues. Alternatively, the pump beam can be steered with respect to the static probe's position.

Similar to other FDTR measurements we compare two measurements to extract the desired thermal phase from additional instrumental contributions that make up the measured phase. Since both signals travel through the same optical and electrical paths, the subtraction of normal and reference measurement gives us the desired phase lag which is then fitted to the diffusive heat equation to extract the in-plane and out of plane thermal conductivities as well thermal boundary conductance with the Al layer.

Given that we work with small spot sizes, the accurate determination of spot sizes and beam offsets is critical to reduce sources of experimental error. Beam offsets and spot sizes are first characterized by razor profiling using a piezoelectric stage. Pump and probe spot sizes are comparable, with $\omega \cong 1.4$ μm. However, since the focal position may vary slightly every time a sample is repositioned, we find that sufficient accuracy is obtained only when the spot sizes are determined at the focal position where a measurement is to be made. This is achieved by offsetting the probe beam with respect to the pump at high modulation frequencies to measure the combined response to the thermoreflectance signal, and finally fitting the obtained profile to a Gaussian curve to extract RMS spot sizes.

3.5 Results and Discussions

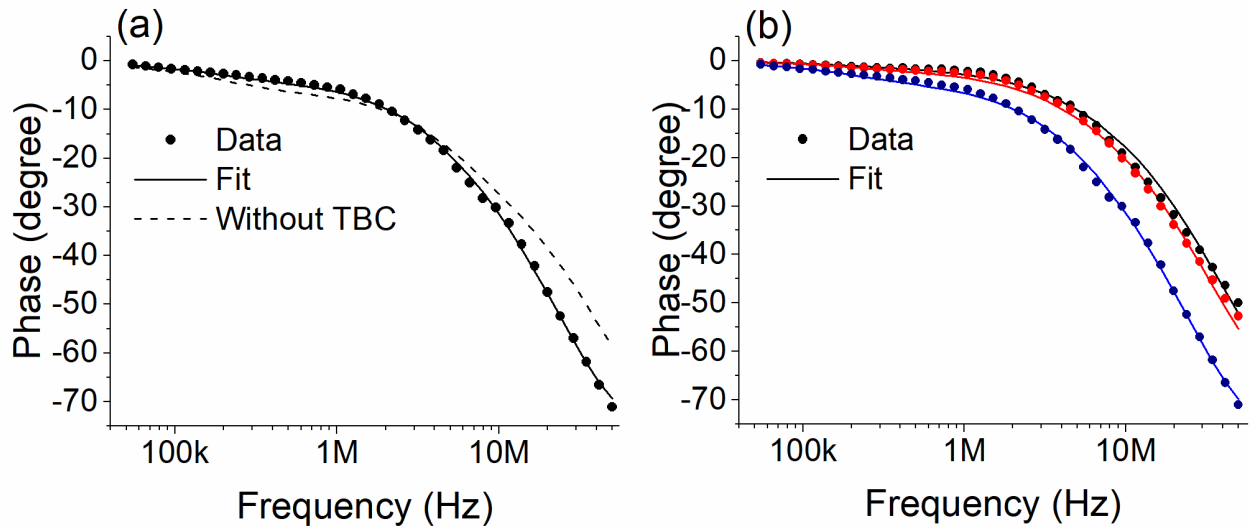

Figure 3. 4 (a) Experimental phase data (symbols) with fitted analytical solution (solid line) on the Al/Graphite sample at 2 μm beam offset. For comparison, the dashed line is the model prediction for the same structure, but without the TBC present at the Al/Graphite interface. Panel (b) shows aggregate data and global fit using 3 beam offset values: 0 μm (black), 1.5 μm (red) and 2 μm (navy).

We have measured the thermal properties of several anisotropic samples by modulating over a wide frequency range from 5 KHz to 50 MHz, and fit $K_{\perp}$, $K_{\parallel}$ and TBC concurrently at 2 μm beam offset. All of the fitted results in this work are summarized in Table 3.2. The experimental data for Al/graphite with fitted analytical solution is shown in Figure 3.4(a). The figure also shows the result of the model in the absence of the thermal boundary at the Al/graphite interface, which shows a deviation from the data mirroring the shape of the sensitivity curve for TBC in fig 3.2(b). The fit yielded $K_{\perp}$= 8 ± 2 W/mK, $K_{\parallel}$= 1,337 ±

176 W/mK and the TBC of Al/graphite of 41 ± 5 MW/m^{2}K. These values agree well with literature data[7,9,73]. We check that there are no dependencies among the fit parameters

*Table 3. 2 Measured values for different anisotropic samples. *: the error bar here represents the confidence interval obtained from 9 measurements. †: the TBC in this case is that of the Al/Graphene/SiO_2 structure.*

Sample	$K_\perp$**(W/mK)**	$K_\parallel$ **(W/mK)**	**TBC with Al (MW/m^{2}K)**
Graphite	6.5 ± 1	1,455 ± 148	47 ± 1
c-plane Sapphire	50 ± 1.2	35 ± 0.6	134 ± 3
a-plane Sapphire	39 ± 2	37 ± 1.1	167 ± 11
r-plane Sapphire	41 ± 2	37 ± 1.2	118 ± 4
Single layer Graphene		707 ± 39*	28 ± 0.5†

by operating on the Variance-Covariance matrix. Note that all error bars indicated in this work are the standard errors obtained from the goodness of fit, and do not incorporate the propagation of uncertainties in the parameters that were held constant during the fit. To improve the standard error of the fit while maintaining self-consistent results, we concurrently fit measurements obtained at multiple offsets as shown in Figure 3.4(b), yielding $K_\perp$= 6.5 ± 1 W/mK, $K_\parallel$= 1,455 ± 148 W/mK and TBC = 47 ± 1 MW/m^{2}K. As can be seen in Figure 3.4(b), the thermal phase lag increases with increasing beam offset value, as indicated in the sensitivity curves of Figure 3.2, in which all sensitivities are

positive and increase with beam offset, i.e. given a set of thermal parameters, increasing the offset increases the change in thermal phase.

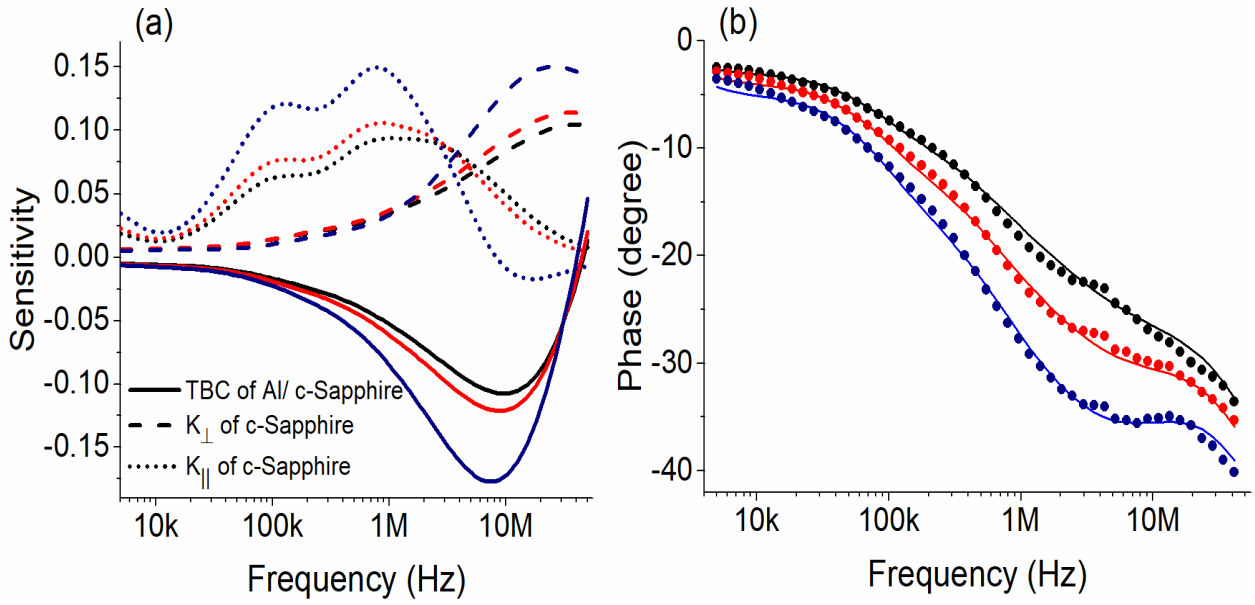

Figure 3. 5 (a): Sensitivity to $K_{\perp}$, $K_{\parallel}$ of c-Sapphire and TBC across Al/c- Sapphire interfaces, for several values of beam offsets. (b) Experimental phase data (symbols) with fitted analytical solution (solid lines) for the Al/c- Sapphire sample. The beam offset values were 1 μm (black), 1.5 μm (red) and 2 μm(navy).

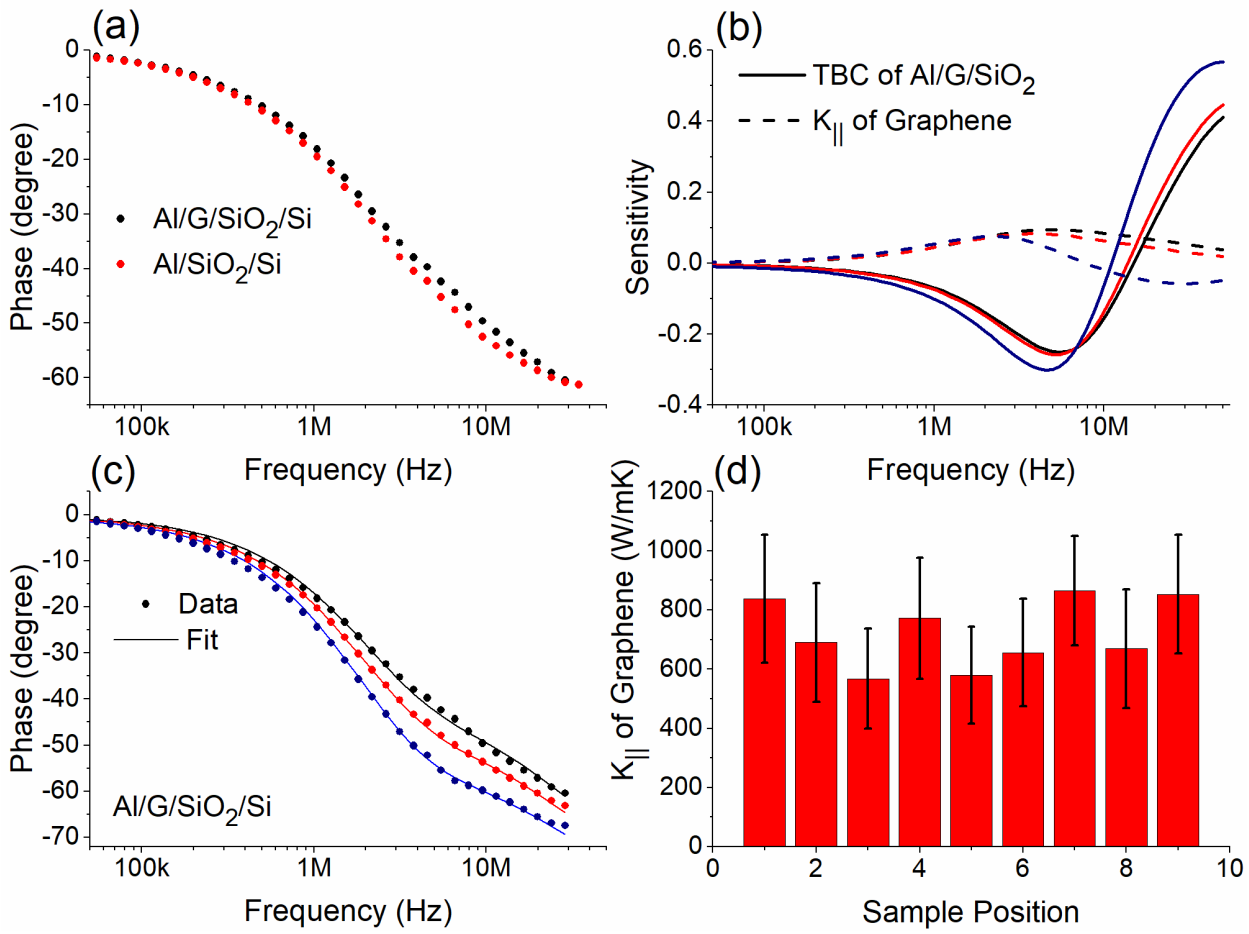

Figure 3. 6 (a) Experimental phase data at 0 μm beam offset for the Al/Graphene/SiO_2/Si sample on an area containing Graphene (black symbols) compared with an area that does not contain Graphene (red symbols). (b): Sensitivity to $K_{\parallel}$ of Graphene and TBC across Al/Graphene/SiO_2 interfaces for the Al/Graphene/SiO_2/Si sample, for several values of beam offsets of 1 μm (black), 1.5 μm red) and 2 μm (navy). (c): Experimental phase data (symbols) with fitted analytical solution (solid lines) for the Al/Graphene/SiO_2/Si sample. The beam-offset values were 0 μm (black), 1 μm (red) and 1.5 μm (navy). (d): $K_{\parallel}$ of single layer Graphene for the structure Al/Graphene/SiO_2/Si extracted from different locations in the sample.

Similar measurements were performed on c-plane, a-plane and r-plane Sapphire to extract the anisotropic thermal conductivity and TBC. Sapphire is anisotropic with a larger thermal conductivity along the c-axis, the value depending on the level of impurities in the crystal. The sensitivity curves in Figure 3.5 (a) show frequency dependencies for the thermal parameters of interest to be quite distinct from each other and increasing with beam offset, indicating that each parameter can be individually determined. The data of Figure 3.5 (b) shows the development of a saddle point before 10 MHz for larger beam offsets, mimicking the increase in sensitivities of opposite sign for K and the TBC. There is a slight feature in our data at 5 MHz which coincides with the onset of coherent RF noise correction (which is performed for this sample at frequencies higher than 5 MHz). Our results for c-plane Sapphire, Figure 3.5(b), show a larger $K_{\perp}$= 50 ± 1.2 W/mK as expected, the value being comparable to that obtained for high-quality crystals[74,75]. On the other hand, the values obtained for the a-plane and r-plane on two other crystals (Table 3.2) do not show an appreciable anisotropy, as expected, since the in-plane and out-of-plane conductivities for these crystal planes are not aligned along the c-axis. The values of TBC of Al/Sapphire are in line with earlier reports[23], and indicate a lower conductance across the Al/r-plane interface, which is consistent with lower sound speeds recorded for this crystal face[76]. Lower sound speeds indicate a flatter acoustic phonon dispersion relation, which dominates the contribution to the TBC.

Finally, we present the in-plane thermal conductivity measurements of single layer CVD graphene (Figure 3.6). The sample structure is Al/graphene/SiO_2(296nm)/Si. The possibility of measuring the presence of monolayer Graphene between Al and the SiO_2/Si support is demonstrated in Figure 3.6(a) where data in a region of the sample without graphene is compared with a region with graphene, yielding an appreciable difference as high as $\sim 5°$, well above the noise of the measurement. Figure 3.6(b) shows the sensitivity to measuring the $K_{\parallel}$ of graphene and the TBC of the combined Al/graphene/SiO_2 interface. Given the large anisotropy in graphene favoring in-plane transport, the presence of the underlying thick, low-conductivity SiO_2 layer beneath it enhances the ability to assess $K_{\parallel}$. From the region where no Graphene was present we determine the TBC at the Al/SiO_2 interface (92 MW/m^{2}K) and at the SiO_2/Si interface (28 MW/m^{2}K), then we fix the TBC at the SiO_2/Si interface and all other parameters to fit $K_{\parallel}$ of graphene and the combined TBC across the Al/Graphene/SiO_2 interfaces by performing beam-offset measurements at different locations of the sample (Figures 3.6 (c) and 3.6 (d)). The TBC values at the Al/SiO2 and SiO_2/Si interfaces are consistent with those of other reports[51,59,77,78]. We model the graphene layer as having a thickness of 0.35 nm and negligible out-of-plane thermal resistance, and treat this together with the TBC of Al/graphene and the TBC of graphene/SiO_2. The TBC across Al/graphene/SiO_2 fit from the data at 9 different locations is 28 ± 0.5 MW/m^{2}K, in line with other measurements[47,79]. This can be decomposed into a contribution of 47 MW/m^{2}K for the Al/graphene interface (approximated from the TBC of Al/graphite measured here), and 69 MW/m^{2}K for the graphene/SiO_2 interface, in accordance with literature values[47,80]. The average value for $K_{\parallel}$ of graphene obtained over 9 locations across the sample is 707 ± 39 W/mK, which is

very similar to the values reported in the literature for supported graphene[26,47,81]. In all cases referenced, the single layer graphene was supported on SiO_2, whereas in the work by Yang the graphene was also covered by Al or Ti[47]. It's interesting to note that our reported value for $K_{\parallel}$ is in line with the literature in spite of the fact that the graphene in this work was obtained by CVD growth, rather than mechanical exfoliation from graphite. The similar values among these studies suggest that $K_{\parallel}$ in supported Graphene is predominantly limited by phonon scattering induced by the SiO_2 substrate, rather than grain boundary scattering within the graphene layer or the presence of a metallic top layer. This is supported by Yang's observation that $K_{\parallel}$ was independent of Al or Ti contact metal[47], and their estimate that for $K_{\parallel}$~700 W/mK, the phonon mean free path in graphene is ~55 nm. This is substantially lower than the crystal domain size of 10-25 μm for the CVD graphene sample used here or the flake sizes in the references cited, supporting the argument that the phonon mean free path is dominated by scattering induced by the SiO_2 substrate.

The results obtained here for graphene demonstrate how BO-FDTR can be effective in determining $K_{\parallel}$ in substrate-supported 2D materials, which is typically challenging. We note that by beam-offsetting and high-frequency measurements we markedly reduced the uncertainties of the derived values. Yang's FDTR approach did not use beam-offsetting, and given the lower sensitivity in the coaxial geometry, it relies on a large number of measurements to reduce the statistical uncertainty of the derived values. Other techniques that have been used to determine the $K_{\parallel}$ in supported graphene include suspended microbridge geometries that are not amenable to systematic studies[81], or

Raman/IR thermometry that don't independently measure the TBC[60,82,83] which affects the value and uncertainty of $K_{\parallel}$.

3.6 Summary

We have measured the in-plane, out-of-plane thermal conductivities and TBC simultaneously over a large range of thermal conductivity values (~5 W/mK to ~1,500 W/mK) in anisotropic samples. High sensitivities are obtained by modulating at high frequencies even at large beam offsets. We note that modulation frequencies of 50 MHz while at an offset of 1.4 times the spot size are the largest reported for beam offset FDTR and facilitate measurement of in-plane transport. The proposed approach to assessing the thermal properties of anisotropic materials will be helpful for device applications that take advantage of the promising qualities of emerging 2D materials.

CHAPTER 4

Thermal Transport in 2D Materials Through FD-MOKE[2]

4.1 Overview

The rapidly increasing number of 2-dimensional materials that have been isolated or synthesized provides an enormous opportunity to realize new device functionalities. Whereas optical and electrical characterization has been more readily applicable to these new materials, quantitative thermal characterization is more challenging due to the difficulties with localizing heat flow. Optical pump-probe techniques that are well-established for the study of bulk materials or thin-films have limited sensitivity to lateral heat transport, and the characterization of the thermal anisotropy that is common in 2-dimensional materials is therefore challenging. Here we present a new approach to quantify the thermal properties based on the magneto-optical Kerr effect that yields quantitative insight into cross-plane and in-plane heat transport. Using a magnetic material as optical transducer allows the use of semi-transparent layers that are very thin, increasing the in-plane thermal gradients. The approach has the added benefit that it does not require the sample to be suspended, providing insight of thermal transport in supported, device-like environments. We apply this approach to measure the thermal properties of a range of 2-dimensional materials which are of interest for device applications, including single layer graphene, few-layer h-BN, single and two layer MoS_2,

[2] This chapter is to be submitted for publication soon with contributions from co-authors M. Shahzadeh and S. Pisana. This chapter has also been presented in APS March Meeting, 2019[84].

and bulk $MoSe_2$ and WS_2 crystals. We detect a large deviation from diffusive heat transport in WS_2, in accordance with first-principle calculations predicting large phonon mean free paths, with important implications for thermal management in device applications.

4.2 FD-MOKE

In spite of the numerous studies that focus on the optical and electrical properties of these 2D materials, the thermal characterization has lagged behind, due to the difficulties with localizing heat flow within the material of interest and obtaining quantitative results. The thermal conductivity of these materials is highly anisotropic because of the strong atomic interactions along the basal plane compared to weak bonding present cross-plane (typically the crystal's *c*-axis). Raman thermometry has been used to measure in-plane heat transport of 2D materials, but the technique is prone to inaccuracies due to errors in accurately determining the optical absorption of the sample and heat transfer at the sample boundaries, the latter being more challenging to quantitatively asses and take into account[85]. As a result, despite the relative simplicity of the Raman technique, a more accurate approach is required, ideally capable of also measuring interfacial heat transport or transport along different directions. The optical pump-probe techniques known as time domain thermoreflectance[6,7,9] and frequency domain thermoreflectance[8,10,22,23,47,63,64] are well established to directly measure the thermal conductivity and thermal boundary conductance (TBC) of bulk materials and thin films[2,3]. These detect changes in the surface temperature of a sample subject to an optically generated heat flux, and the

results are used to extract the thermophysical properties of interest. However, these techniques are not normally sensitive to lateral heat transport, and hence the characterization of anisotropic 2D materials is very challenging. The in-plane thermal conductivity of some anisotropic materials has been measured through thermoreflectance techniques by beam offsetting[7,10,63] and varying spot sizes[9]. The experimental sensitivity needs to be further increased to measure the anisotropic thermal conductivity as well as TBC of these 2D materials, especially for the case of single and multilayer structures. Jun Liu et al. recently demonstrated how using a thin transducer enhances the sensitivity to lateral heat transport in time domain thermoreflectance (TDTR)[58]. However, in TDTR the instrumentation is comparatively expensive, and the measurements are typically modulated at frequencies below 20 MHz, setting a lower limit to the thermal penetration depth and in turn limiting the ability to measure thin samples. Frequency domain thermoreflectance (FDTR) is cost effective as it does not require a mechanical delay stage, an ultrafast laser or electro-optic modulators, and allows modulating the measurement over a wide range of frequencies[10].

In this work we implement frequency domain magneto-optical Kerr effect (FD-MOKE), a new approach to quantify the thermal properties of anisotropic materials based on the Kerr effect, yielding enhanced sensitivity to lateral heat transport. While in FDTR the sample is typically coated with a relatively thick 50-100 nm metal film with large thermoreflectance coefficient (known as the transducer), in FD-MOKE a thinner magnetic film is used as a transducer and the detection of the modulated surface temperature is achieved through the Kerr effect through changes in magnetization as function of temperature $\frac{dM}{dT}$[58]. Reducing the thickness of the metallic layer limits the lateral heat flow

within it and increases the sensitivity to lateral heat flow in the sample. Additionally, a thinner transducer has a lower thermal mass and can be used to probe heat transport over shallower depths. Reducing the transducer thickness in typical thermoreflectance approaches is not convenient, as the interpretation of the results either requires that all the optical energy be absorbed within the transducer, or a more complicated model is needed to account for the optical properties and absorption as function of depth. Kerr detection on the other hand is only sensitive to changes in the magnetization state of the magnetic layer, so any optical contribution from other layers are not detected and do not contribute to the measurement.

Applying FD-MOKE and beam offset FD-MOKE, we have measured the thermal properties of a range of 2-dimensional materials including single-layer graphene, few-layer h-BN, single and two-layer MoS_2, and bulk $MoSe_2$ and WS_2 crystals. The thermal properties of bulk silicon and sapphire are also measured as reference to demonstrate the validity of this technique.

4.3 Sample Preparation and Materials Characterization

Graphene, h-BN, MoS_2, WS_2 and $MoSe_2$ samples were obtained from 2D Material, whereas Si and Al_2O_3 from MTI. Graphene, h-BN and MoS_2 were few-layer polycrystalline films synthesized through chemical vapor deposition and subsequent transfer to SiO_2(300 nm)/Si substrates. All samples were coated with a 20 nm Nickel film capped by 3 nm of Aluminum by sputter deposition. The Al layer prevents oxidation of the Ni layer. White light interferometry was used to measure the layer thickness. Electrical conductivity

measurements were done by a 4-point probe to calculate the thermal conductivity of the metal layer via the Wiedemann-Franz law. A clean surface of the $MoSe_2$ and WS_2 crystals was obtained by exfoliation with adhesive tape.

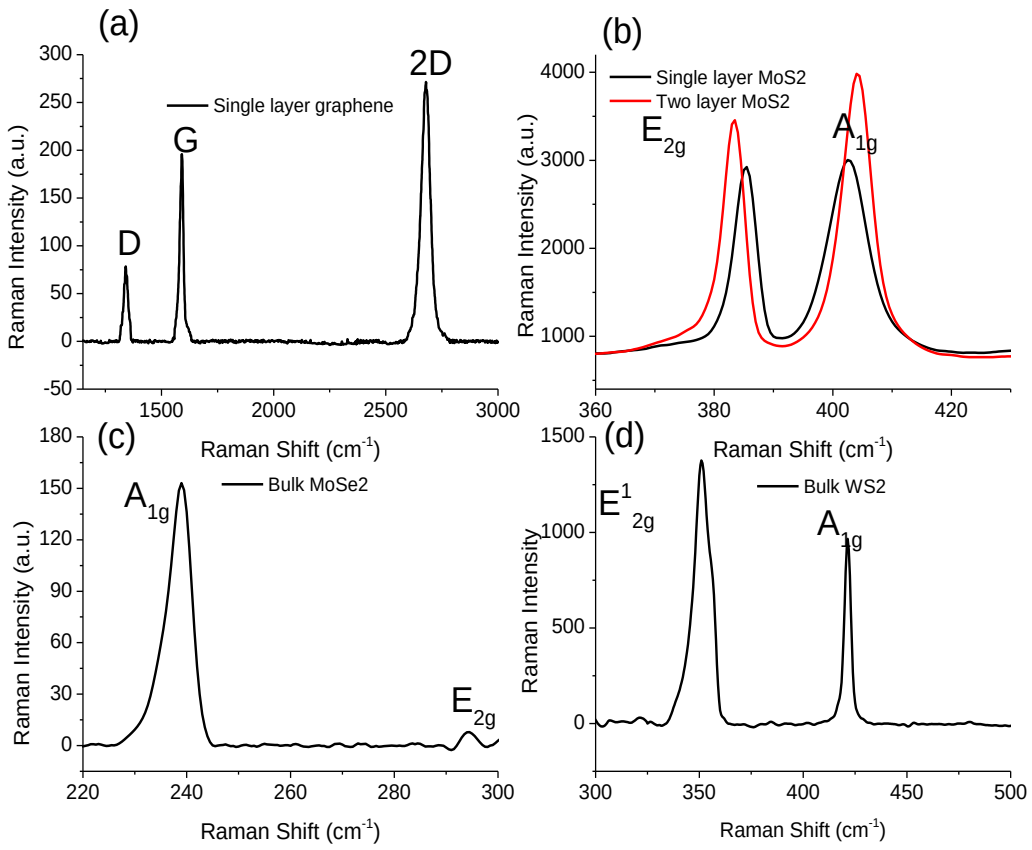

Figure 4. 1 Measured Raman Spectra of the 2D materials in this study

We measured the Raman spectra for the single-layer graphene, few-layer h-BN, single and two-layer MoS_2 samples on SiO_2/Si substrate and bulk $MoSe_2$ and WS_2 using

a Bruker Senterra dispersive Raman microscope at 532 nm. A 50X objective is used with a range of power from 5 mW to 10 mW. Figure 4.1(a) illustrates the Raman spectra of single-layer graphene where the G peak and 2D peaks are observed near 1591 cm^{-1} and 2679 cm^{-1} respectively. The observed D peak indicates the presence of defects that can be associated with grain boundaries in a polycrystalline sample. The 2D peak is a sharp Lorentzian peak with a full width at half maximum of 44 cm^{-1}, and it is more intense than the G peak, identifying single-layer graphene[86,87]. The comparison of the single and two-layer MoS_2 is shown in Figure 4.1(b), where the in-plane and out-of-plane mode peaks for the two-layer sample are at 383.5 cm^{-1} and 404.5 cm^{-1}, respectively, which upshift and downshift, respectively, for the single-layer[88–90]. In Figure 4.1(c), the out-of-plane vibrational mode for bulk $MoSe_2$ is observed at 240 cm^{-1}, whereas the weaker in-plane vibration mode is found at 295 cm^{-1} [88]. Also, in Figure 4.1(d), the in-plane phonon mode for bulk WS_2 is observed at 351 cm^{-1} and the weaker out-of-plane mode is found at 422 cm^{-1}, in agreement with previous result[91]. In the case of h-BN excited with a laser in the visible range, the Raman processes are non-resonant and consequently, Raman spectra are much weaker[92]. The number of layers for the two of the h-BN samples was estimated through AFM characterization by measuring the step height with respect to the SiO_2/Si substrate and found to be 4 layers (~2nm) and 20 layers (~9nm).

4.4 Sensitivity Analysis

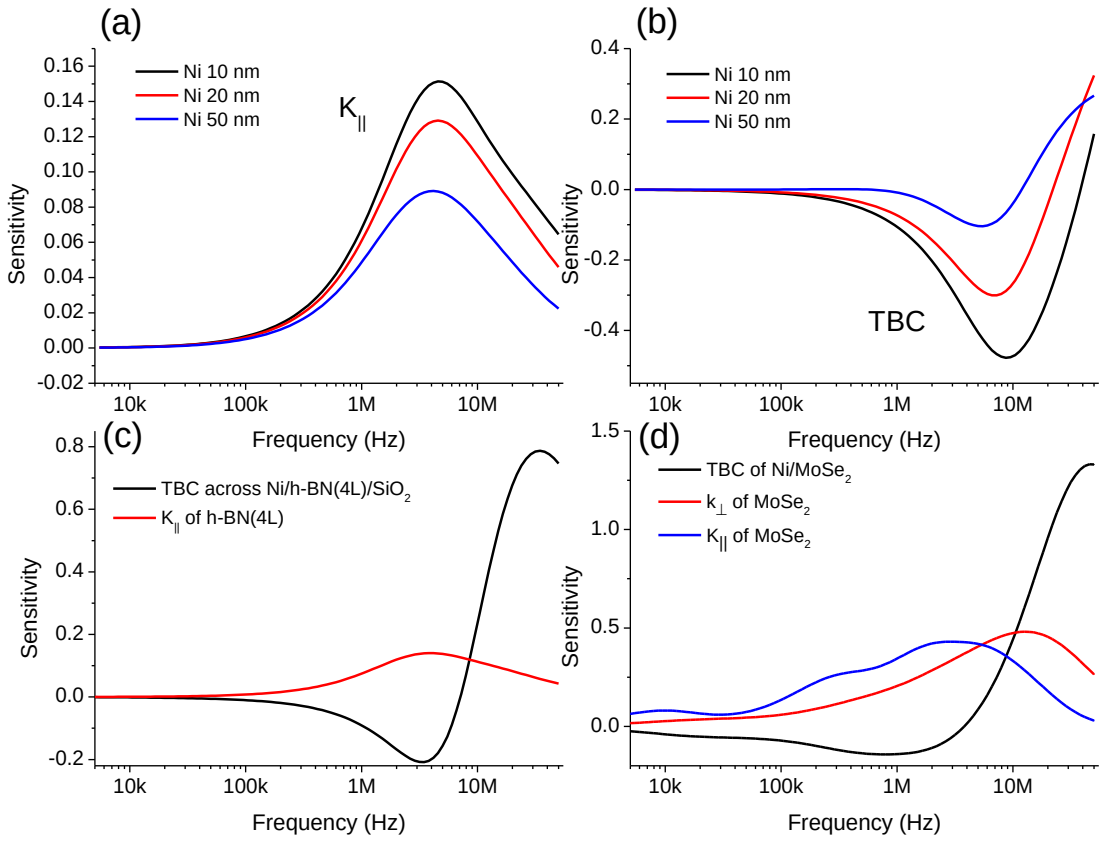

Figure 4. 2 (a) and (b) plot the sensitivity of the measured thermal phase to the in-plane thermal conductivity of single-layer graphene and the TBC across the Ni/graphene/SiO_2 interfaces for several values of the transducer thickness. (c) and (d) show the sensitivity to the measured thermal phase to changes in different parameter using a 20nm Ni transducer.

We first consider the ability to sense single-layer graphene on a SiO_2/Si substrate. Figures 4.2 (a) and (b) illustrate how a thin transducer layer enhances the sensitivity to measuring

the in-plane thermal conductivity of single-layer graphene and the effective TBC across the metallic layer/graphene/SiO_2 interfaces, respectively. The distinct spectral sensitivity of various parameters, as also shown for example in Figures 4.2 (c) and (d) for the in-plane thermal conductivity of 20-layer h-BN and the TBC across the Ni/h-BN/SiO_2 interfaces, or the anisotropic thermal conductivity of $MoSe_2$ and TBC of the Ni/$MoSe_2$ interface allow us to determine these parameters concurrently.

4.5 Experimental Method

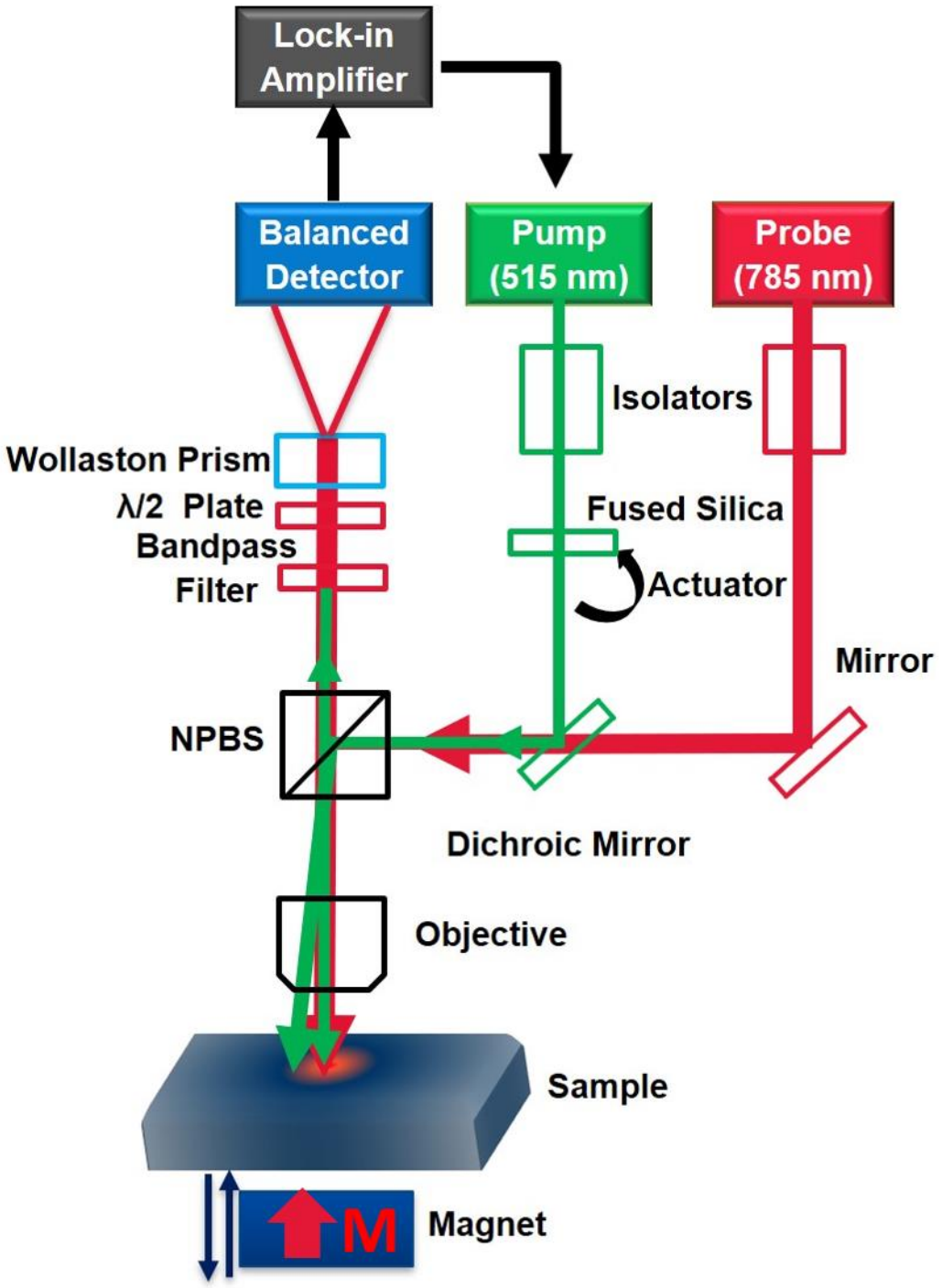

Figure 4. 3 Schematic diagram of the Frequency Domain Magneto-Optical Kerr Effect setup

The basic operating principle in FDTR and FD-MOKE is to impose a sinusoidal heat flux on the sample surface and detect the resulting surface temperature oscillations. The phase shift between the heat flux and the temperature oscillations are proportional to the thermophysical properties of the sample. The main difference is that FDTR samples the surface temperature through thermoreflectance $\left(\frac{dR}{dT}\right)$, whereas FD-MOKE captures the thermally-induced changes in magnetization $\left(\frac{dM}{dT}\right)$. The experimental setup of FD-MOKE as illustrated in Figure 4.3 is similar to that of FDTR[10,64] but with a different detection scheme. Briefly, a sinusoidally modulated pump beam and continuous wave probe beam are combined and focused on the sample surface. Non-polarizing optics are used to route the beams in order to avoid affecting the strength of the Kerr signal. A Wollaston prism splits the beam into two orthogonal polarization states, and a half-wave plate balances their intensities before reaching a balanced photodetector. We offset the pump beam with respect to the probe using a 12 mm thick fused silica plate on an actuated optical mount. Optical spot sizes with $1/e^2$ rms values of 1.4 μm are achieved through a 40X objective, and increase the signal strength allowing us to detect signals over a wide range of frequencies up to 50 MHz. The accurate determination of the spot sizes is critical to minimize error, and this is done by profiling the beams at their focal point across the sharp sample's edge using a piezoelectric state.

The optical system is set-up in the polar Kerr configuration for ease of implementation, and this implies that the detected signal is sensitive to changes of the magnetization state of the transducer in the direction perpendicular to the sample surface. In this case, transducer materials with perpendicular magnetic anisotropy would be ideal, but this would also complicate sample preparation. We choose to use Nickel thin films as

transducer for several reasons. First, Ni is readily available and a thin film with repeatable magnetic characteristics can be easily deposited irrespective of the choice of substrate or film thickness. Since the demagnetizing field of the thin film dominates any other source of anisotropy, the remanent magnetization will be in-plane. In order to achieve Kerr contrast in the polar geometry, the magnetization needs to be brought out of the plane of the sample, so using Ni, which is a ferromagnet with relatively low magnetization ~500 emu/cc, a relatively weak field of ~6.3 kOe is sufficient to tilt the magnetization out of the plane. Lastly, Ni has a relatively low Curie temperature ~350 C, therefore its magnetization curve as function of temperature will have a comparatively large slope dM/dT near room temperature, aiding in the measurement of the temperature induced changes to the magnetization. A 20 nm Nickel layer serves as a transducer throughout this work, but thinner layers can also be used.

To isolate the thermal phase lag of interest, we perform two measurements of the phase of the signal as function of modulation frequency. We first null the probe signal in the balanced detector by rotating the half-wave plate, then we perform the first measurement while applying a saturating perpendicular field to the sample using an external permanent magnet. This measurement is referred to as θ_1, and it contains the phase information from the temperature fluctuations in the magnetic layer, reference phase, optical phase, and electrical phase. Since the measurement was preceded by nulling the probe signal at zero applied magnetic field, only the response from the magnetic transducer contributes to the signal, whereas any other contribution such as thermoreflectance from underlying layers is rejected. Another measurement is required to determine the reference phase, and optical and electrical contributions. This

measurement is referred to as θ_2, and is performed by detecting the pump beam. Subtracting the two measured phases ($\theta_1 - \theta_2$) yields the desired thermal phase, which is fit to a model based on the diffusive heat equation to extract the thermal properties of interest. Two optical bandpass filters are used to separate the pump and probe beams before the balanced photodetector.

4.6 Uncertainty Estimation

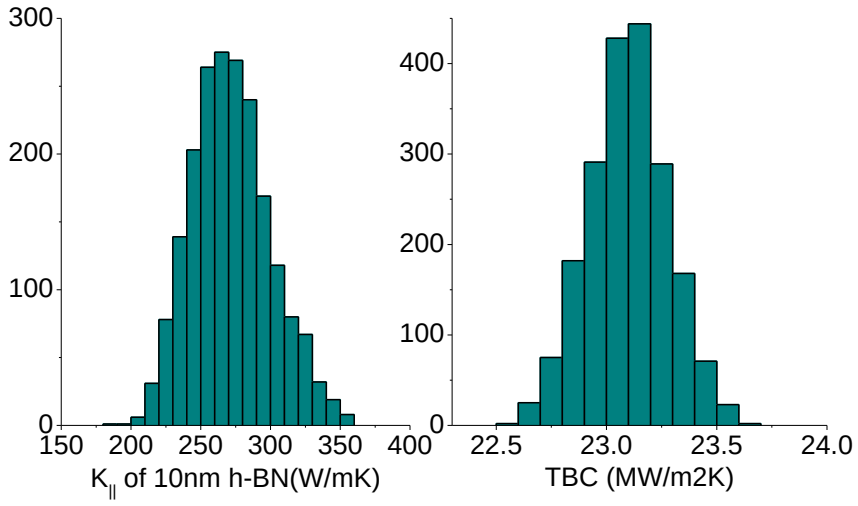

Figure 4. 4 Monte Carlo histograms for the 20-layer h-BN sample

In spite of the optical spot size measurements we perform, small changes in the assumed value affect the derived thermal properties of single and few-layer materials more than for the case of single crystal samples. Additionally, errors in the measurements of the NI film thickness and its electrical conductivity, or deviations in any of the other parameters

from their true value can increase the uncertainty. We estimate the propagation of these errors by a Monte Carlo approach, where random errors are introduced in the assumed parameters and the data to estimate the variation on the derived properties. The standard deviation in optical spot size is estimated from several independent measurements to be 3%. Additionally, the uncertainty in the measured phase originating from experimental noise of 0.1 degree is also included. 2000 Monte Carlo runs were used until the results converged. For each Monte Carlo run both the fitted parameters and goodness of fit were recorded, the latter was used to weigh the value of its associated parameter for statistical significance. We than calculated the weighted average and standard deviation. As an example, the resulting Monte Carlo histograms of in-plane thermal conductivity and effective conductance of Ni/graphene/SiO_2 for 20-layer h-BN sample is shown in Figure 4.4.

4.7 Results and Discussions

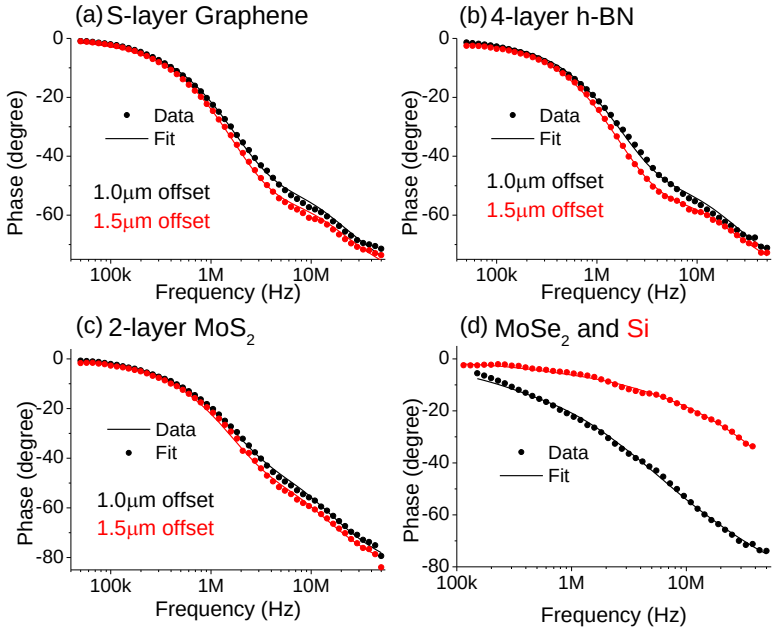

Figure 4. 5 Panels (a), (b), and (c) show aggregate data (symbols) and global fit (solid lines) using 2 beam offset values: 1 μm (black) and 1.5 μm (red) for the Ni/graphene(1L)/SiO_2/Si, Ni/h-BN(4L)/SiO_2/Si, and Ni/MoS_2(2L)/SiO_2/Si samples, respectively. (d) data and fit at 1 μm offset for the Ni/$MoSe_2$ crystal (black) and at 0 μm offset for Ni/native SiO_2/Si (red) samples, respectively.

We have measured the anisotropic thermal conductivity as well as effective thermal boundary conductance between the Ni layer and several sample/substrate combinations by modulating over a wide frequency range from 50 KHz to 50 MHz through concentric and beam offset frequency domain magneto-optical Kerr effect. All the parameters fitted from these measurements are presented in Table 4.1 and representative data with fits are presented in Figure 4.5. Reference measurements were carried out on two standard crystal samples, Silicon and Sapphire, to verify the validity of the FD-MOKE technique.

For Silicon (which includes its native oxide layer) we obtained a thermal conductivity of 123 ± 2 W/mK and a TBC with Ni of 134 ± 3 W/mK. The value for the TBC of Ni/Si is expected to be similar to that of the Al/Si interface, as one would expect from the similar phonon dispersion properties of Al and Ni[93]. The value obtained is in line with other reports[23], though the value varies according to sample preparation. The measured thermal conductivity of Si is ~15% lower than that expected for the bulk intrinsic crystal, and this is because these measurements were performed with a small pump/probe optical spot size, which is known to manifest itself in a reduced apparent thermal conductivity due to the onset of non-diffusive heat transport[53] in crystals having very long mean free path heat carriers. The result obtained here is in line with the non-diffusive heat transport reported by Wilson and Cahill at comparable spot sizes[53]. The presence of the native oxide is expected to cause the reduction in the apparent thermal conductivity to be more sensitive to spot size rather than modulation frequency, given our experimental conditions[66]. For Sapphire the thermal conductivity is in agreement with literature values, though the weak anisotropy (<10%) expected along the *c*-axis is not captured well within the sensitivity of this measurement. The TBC at the Ni/sapphire interface is lower than expected[93,94], as the Al/sapphire TBC is near 250 MW/m^{2}K. Although our value is comparable to that of other reports[10,23], the reduced value observed here may be affected by adsorbates on the sapphire surface prior to the Ni deposition.

Table 4. 1 Measured values for different samples. [a]: The error bar here represents the standard deviation obtained from Monte Carlo simulations. [b]: the TBC, in this case is across the Ni/sample/SiO_2 interfaces.

Sample	$K_{\perp}$**(W/mK)**	$K_{\parallel}$ **(W/mK)**	**TBC with Ni (MW/m^{2}K)**
Single-layer graphene[a]		636 ± 140	17 ± 0.2[b]
Singe-layer MoS_2[a]		63.1 ± 22.6	15 ± 0.2[b]
Two-layer MoS_2[a]		74.2 ± 10.1	13 ± 0.2[b]
4-layer h-BN[a]		242 ± 21.9	20 ± 0.3[b]
20-layer h-BN[a]		270 ± 28.2	23 ± 0.2[b]
$MoSe_2$ crystal	1 ± 0.1	30 ± 2	24 ± 1
WS_2 crystal	3 ± 0.3	38 ± 4	14 ± 1
Sapphire	32 ± 2	37 ± 2	180 ± 20
Silicon	123 ± 2	123 ± 2	134 ± 3

As shown in Figure 4.2(d), we have enough sensitivity to the anisotropic thermal conductivity in $MoSe_2$ as well as TBC of the Ni/$MoSe_2$ interface, and hence we can measure these three parameters concurrently. The experimental data with the analytical fitted solution is in Figure 4.5 (d) and the fit yields in and out-of-plane thermal conductivity of $MoSe_2$: $K_{\perp}$= 1 ± 0.1 W/mK and $K_{\parallel}$= 30 ± 2 W/mK respectively, and the TBC of Ni/$MoSe_2$ of 24 ± 1 MW/m^{2}K. The measured thermal conductivity is highly anisotropic as expected

from the weaker atomic bonding along the *c* axis, and is in agreement with the reported in-plane thermal conductivity of a 80 nm thick $MoSe_2$ film (25.7 ± 7.7 W/mK)[95]. Our data can be compared to first-principles calculations of bulk $MoSe_2$[96], reported to be $K_{\perp}$= 3.5 W/mK and $K_{\parallel}$= 40 W/mK respectively. The discrepancy with respect to theory likely originates from extrinsic effects not included in the first-principles calculations[96] such as crystal defects and boundary scattering. The measured thermal boundary conductance of 24 ± 1 MW/m^{2}K is very low compared to typical metal dielectric interfaces, but this is common for layered crystals, and in good agreement with the measurement for MoS_2[58]. The low thermal boundary conductance has been ascribed to the effect of phonon focusing in crystals with elastic anisotropy[97].

Although there are several reports for the thermal properties of single-layer WS_2, the measured values are inconsistent with predictions. The thermal of single-layer WS_2 is calculated from first-principles to be near 150 W/mK, and the values for the bulk crystal are expected to be 140 W/mK in the basal plane and 4.7 W/mK across it[96,98]. However, through Raman scattering the measured value are found to be 32 W/mK for single-layer WS_2 and 52 W/mK for bilayer WS_2[46]. There appears to be only a report on the bulk thermal properties of WS_2, which indicates a basal plane conductivity $K_{\parallel}$ of 124 W/mK and a $K_{\perp}$ of 1.7 W/mK. Here we measure the bulk WS_2 crystal to have $K_{\perp}$= 3 ± 0.3 W/mK, $K_{\parallel}$= 38.2 ± 3.9 W/mK, and the TBC across Ni/WS_2 of 14 ± 1 MW/m^{2}K. Our measured in-plane thermal conductivity appears to be much lower than expected. Unlike the case of $MoSe_2$ above, were the smaller (~25%) discrepancy was attributed to boundary scattering, a similar contribution in WS_2 could not account for the ~75% reduction observed here. We believe that the difference can instead be attributed to the unusually large mean free

paths in the WS_2 crystal[96], where phonons with mean free path greater than 1 μm contribute to 95% of the in-plane thermal conductivity. Given our 1.4 μm optical spot size, it appears that the measurements are affected by strong deviations from Fourier heat transport which suppress the apparent thermal conductivity. Such an effect would not be as strong in the $MoSe_2$ sample above, as theory finds that the contribution to thermal conductivity in selenide crystals originates from phonons of shorter mean free path compared to sulfide crystals[96]. The deviation from diffusive transport cannot be attributed to the effect of weak-electron phonon coupling in the Ni layer, in contrast with measurements made using Au transducers[99,100]. This result highlights the dramatic effect nanoscale heat transport can have on the ability of materials to transport heat, and can have profound implications for device applications.

We now move to measurements made on few-layer 2D materials. For these cases, the determination of the in-plane thermal properties is challenging, particularly for materials with relatively small in-plane thermal conductivity, due to the low sensitivity to in-plane heat transport. Measurements on graphene have been reported before[10,47], and the approach with FD-MOKE presented here can serve to verify the validity for measurements on these ultra-thin layers. Here, the use of a thin transducer enhances the sensitivity to lateral heat transport. As seen in Figures 4.2(a) and (b) the experiment has enhanced sensitivity to the in-plane thermal conductivity of single-layer graphene and effective thermal boundary conductance across the Ni/graphene/SiO_2 structure. We model the graphene layer as having a thickness of 0.335 nm and negligible out-of-plane thermal resistance and treat this together with the TBC of Ni/graphene and the TBC of graphene/SiO_2. We performed measurements at several offsets, and the fitted value for

$K_{\parallel}$ of graphene is 636.6 ± 140 W/mK and the TBC across Ni/graphene/SiO_2 is 17 ± 0.2 MW/m^{2}K. The measured in-plane thermal conductivity is in good agreement with our previous measurement through beam offset FDTR[10] and with other literature values[26,47,81]. The TBC across Ni/graphene/SiO_2 can be decomposed into a contribution of 47 MW/m^{2}K for the Ni/graphene interface considering similar Metal/graphene conductance, and 27 MW/m^{2}K for the graphene/SiO_2 interface. Interestingly, all the previous measurements were done using Al or Ti transducers, and here using a Ni transducer we obtained a very similar thermal conductivity. This further strengthens the idea of Yang's observation that the in-plane thermal conductivity of graphene is independent of the metal contact[47]. The reduction of the in pane thermal conductivity in a SiO_2-supported geometry as opposed to a suspended geometry is due to boundary scattering from the SiO_2, and it is expected that this could be enhanced by replacing the SiO_2 support with h-BN.

We now move to few-layer h-BN. As shown in Figure 4.2(c), the measurement sensitivity to both in-plane thermal conductivity and effective TBC across the Ni/h-BN/SiO_2 interfaces is comparable to the case of graphene. We perform these measurements for a 4-layer h-BN film by performing measurements with several beam offsets (Figure 4.5(b)). We model the 4-layer h-BN as an interface having a thickness of 1.33 nm and negligible out-of-plane thermal resistance and treat this together with the TBC of Ni/h-BN and the TBC of h-BN/SiO_2. The fit yields $K_{\parallel}$ of h-BN to be 242 ± 21.9 W/mK, and the TBC across Ni/h-BN/SiO_2 to be 19.6 ± 0.3 MW/m^{2}K. We also measured the thermal properties of a 20-layer h-BN film with several beam offsets and obtained $K_{\parallel}$ of 270 ± 28.2 W/mK, and TBC across Ni/h-BN/SiO_2 of 23.1 ± 0.2 MW/m^{2}K. The measured

thermal conductivity is lower than the reported bulk value of 390 W/mK[48] at room temperature but in line with the reported 250 W/mK value obtained for 5 layers[101], 227–280 W/mK for 9 layers[102], and 360 W/mK for a 11-layer h-BN sample[101]. Similarly to these reports, we also find an increasing trend for the in-plane thermal conductivity of h-BN with the number of layers. The dependence with sample thickness has been ascribed to surface scattering, which is reduced for thicker films.

For the case of MoS_2, the thermal conductivity of the bulk crystal was measured to be between 85–110 W/mK as a function of laser spot size through TR-MOKE[58]. However, there is a large discrepancy in the reported values for single and two-layer MoS_2, and there is no apparent systematic trend for the reported thermal conductivity as function of the number of layers. We performed measurements on single and two-layer MoS_2 (Figure 4.5 (c)) for several beam offset values. The fit gives $K_{\parallel}$ of 63.12 $\pm$ 22.16 W/mK and TBC across Ni/ MoS_2/SiO_2 of 15 ± 0.2 MW/m^{2}K for single-layer MoS_2 and $K_{\parallel}$ of 74.2 ± 10.1 W/mK and TBC of 13 ± 0.2 MW/m^{2}K for the two-layer MoS_2. The relatively large uncertainty in the single-layer film is due to the reduced in-plane heat flux in this structure. The trend of $K_{\parallel}$ with thickness is opposite to the values of 84 W/mK for single-layer MoS_2 and 77 W/mK for two-layer MoS_2 measured by Raman optothermal technique[103] and the prediction from first-principles calculations[104]. The apparent discrepancy may be due to larger error in the value obtained for single-layer MoS_2, or due to scattering induced by the supporting SiO_2, as literature data on 1- and 2-layer MoS_2 is obtained for suspended samples.

4.8 Summary

We have implemented a new technique, frequency domain magneto-optical Kerr effect (FD-MOKE) to enhance the sensitivity to lateral heat transport and measure the thermal conductivity of anisotropic materials including atom-thick materials. Using this technique, we measured the anisotropic thermal conductivity of a wide range of 2D materials which are interest for novel device applications. We performed the first experimental study on bulk $MoSe_2$ crystal, and our measured value is in good agreement with recently reported nm thick $MoSe_2$ film. The suppressed apparent thermal conductivity of bulk WS_2 crystal indicates strong deviations from Fourier heat transport which is due to the small optical spot size and high-frequency modulation and agrees well with theory. Due to the enhancement in experimental sensitivity, we are also able to perform measurements on single, and few-layer 2D materials and measured conductivities are comparable to that of bulk and will provide guidance towards the design of emerging devices based on 2D layered materials. Overall, this technique will allow more robust measurements on 2D layered materials including one-atom thick films and the measured values will provide a better understanding of the heat dissipation problems in the thermal management of nanoelectronic and optoelectronic devices based on these materials.

CHAPTER 5

Thermal Transport in Printed Films of 2D Inks[3]

5.1 Overview

Graphene and other 2-dimensional (2D) materials are the subjects of intense research due to their distinct properties and potential applications particularly in electronics and optoelectronics[34–37]. Solution-processed 2D materials can accelerate the progress even further due to their compatibility with flexible substrates, large scale, and low-cost device fabrication[11,12,14]. In addition, printed films of such inks could have potential use in thermal and thermoelectric applications. However, very little is known about the thermal properties of 2D-materials based inks due to the challenge and complexity associated with measuring their thermal properties, which are highly anisotropic. In order to develop applications based on the thermal properties of 2D-materials based inks, it is of fundamental importance to understand the relation between structure and property, and to determine how electron and heat transport relate in 2D materials. Here, we present simultaneous anisotropic thermal conductivity and thermal boundary conductance (TBC) measurements of graphene, h-BN, and MoS_2 thin films, produced by ink-jet printing of water-based 2D-materials inks[13]. The measured in plane thermal conductivity is surprisingly found to be independent of intrinsic properties and film thickness, and is mainly limited by flake to flake attachment and flake size. High thermal anisotropies are

[3] This chapter will be submitted for publication with contributions from co-authors K Parvez, C Dun, C Casiraghi, and S. Pisana. This chapter has also been presented in APS March Meeting, 2019[105].

observed together with ultra-low cross-plane thermal conductivity well below 0.5 W/mK which is even smaller than the minimum predicted thermal conductivity for these materials. The ultralow thermal conductivity of these disordered materials is induced by the random stacking of individual flakes and layer spacing and might have potential applications in thermal and thermoelectric. Enhancement in both electrical and in-plane thermal conductivities are observed with annealing at different temperatures.

5.2 Sample Preparation and Sensitivity Analysis

Graphene, h-BN, and MoS_2 ink samples were prepared over a range of thicknesses by inkjet printing liquid phase exfoliated crystals on the surface of an oxidized Si wafer with a thick oxide layer[13]. The thickness of the thin films was varied by changing the number of printing passes. The effects of annealing on thermal and electrical conductivities of these films were observed by vacuum annealing at 150°C and at 300°C. To perform the thermal conductivity measurements, these films were coated with (40-50nm) Al transducers by sputter deposition and the Al thickness was measured by white light interferometry or picosecond acoustics. The thermal conductivity of the metal layer was calculated from 4-point probe electrical measurements via the Wiedemann-Franz law.

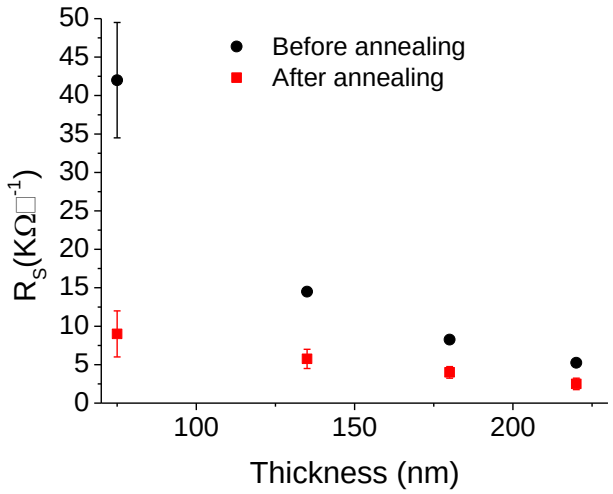

Figure 5. 1 Sheet resistance as a function of the thickness of the graphene films printed on Si/SiO_2 substrate before and after annealing.

We measured the sheet resistance of the graphene films before and after annealing. The sheet resistance of the graphene thin films decreases with increasing thickness and also there is a significant decrease in sheet resistance on the annealed sample as shown in Figure 5.1. The substantial increase (~200%) in electrical conductivity with annealing suggests that improved bonding between adjoint sheets significantly reduces the barrier to electron conduction.

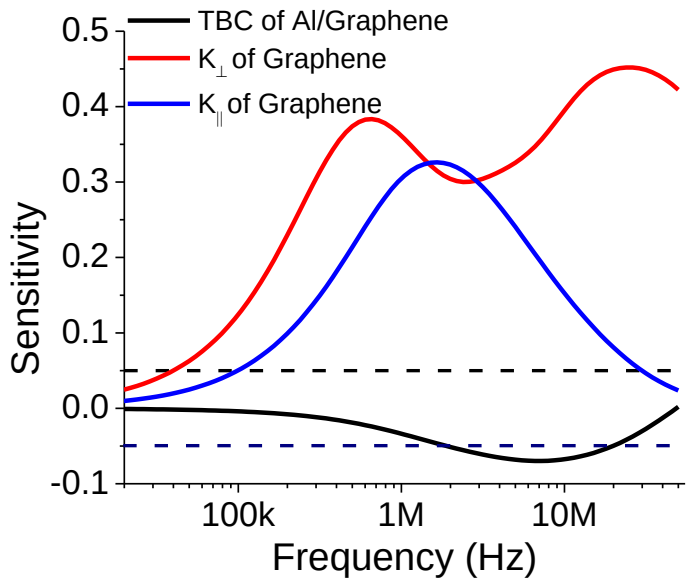

Figure 5. 2 depicts the sensitivity of the measured thermal phase to changes in various parameters on Al(40nm)/Graphene(225nm)/SiO2/Si structure.

In thermoreflectance measurements, the sensitivity analysis tells us how a parameter influences the measurement response. In order to fit an unknown parameter in the diffusive model, this parameter should be very sensitive (>0.05) and distinct from the other parameters, otherwise it can lead to substantial uncertainties in the derived values. We considered an Al(40nm)/graphene(225nm)/SiO_2/Si system to analyze sensitivity to different parameters. The sensitivity of the measured thermal phase signal due to in-plane and out of plane thermal conductivities of graphene and TBC of Al/graphene is depicted in Figure 5.2 for a wide range of modulation frequencies. These three parameters have high sensitivities and are also easily distinguishable because of their distinct frequency dependence. Hence, we can fit these three parameters simultaneously and extract three parameters from a single concentric measurement

without the necessity of incorporating other techniques like beam offsetting or heterodyning. The sensitivity to anisotropic thermal conductivity and TBC for other printed films measured in this paper is similar to that of graphene.

5.3 Thermal Conductivity Measurements

We employed frequency domain thermoreflectance technique (FDTR) to measure the thermal properties of these printed films. In our FDTR system, the phase lag between heat flux generated by a pump laser and the surface temperature rise of the sample observed by a reflected probe laser is measured ,which contains information about the thermal properties of the sample. The phase lag is then used to extract unknown thermal properties of the sample by fitting this measured temperature response to the solution of the heat diffusion equation[6,7,9]. Reduction of the laser spot's size to ~1.5 microns allows us to perform FDTR over a wide range of frequencies from 50 KHz to 50 MHz, which increases the sensitivity to anisotropic thermal conductivity of the films and thermal boundary conductance (TBC) between the films and the Aluminum layer deposited above it to perform the thermal measurements. Consequently, the in-plane and cross-plane thermal conductivities of the three printed films and their TBCs are measured concurrently. Experimental data with the analytical fitted solution for the h-BN film is shown in Figure 5.3 and is representative.

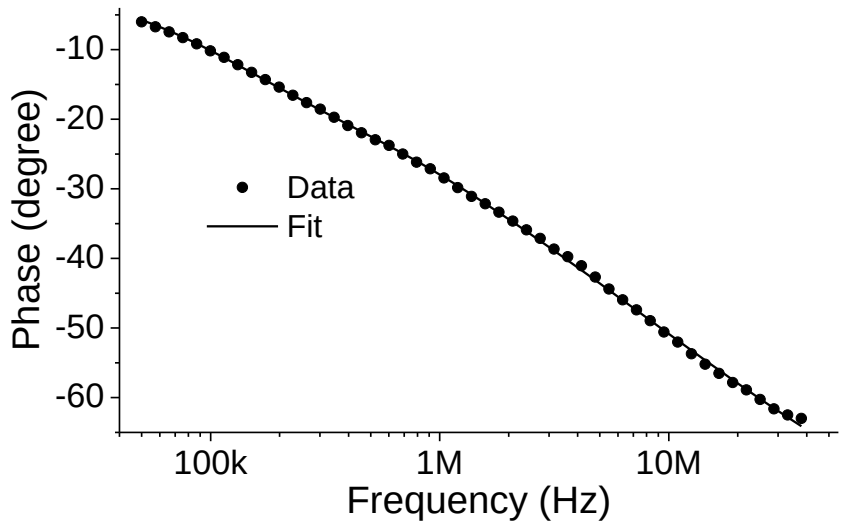

Figure 5. 3 Experimental phase data (symbols) with fitted analytical solution (solid lines) for the Al/h-BN/SiO_2/Si structure.

5.4 Results and Discussions

At first, we performed direct measurements through FDTR on a series of pristine and annealed graphene films over a range of thickness values (231nm-424nm). The measured in-plane and out of plane thermal conductivities are found independent of thickness (Figure 5.4 a)) which is due to the dominance of diffusive phonons with short mean free paths. The overall in-plane thermal conductivity of graphene film is found to be 8.5 ± 0.1 W/mK. However, an increasing trend in in-plane thermal conductivity of graphene film is observed with annealing as a function of temperature. The in-plane thermal conductivity of graphene film with annealing increased to 11.5 ± 0.2 W/mK at 150 °C and 13.38 ± 0.2 W/mK at 300 °C (Figure 5.4(a)). We then performed another set

of measurements on a thinner series of graphene films (75nm-220nm) and did not observe any thickness dependency and got an average in-plane thermal conductivity value of 9 $\pm$ 0.2 W/mK before annealing and 11.1 $\pm$ 0.2 W/mK after annealing at 150 °C (Figure 5.4(b)). The annealing is likely to remove water residues and to thermally degrade the binder and pyrene that were present in the ink. The improvement in thermal conductivity with annealing at 300°C is maximum at about 50%, a modest improvement compared to the more than 200% improvement in electrical conductivity. The increase in thermal conductivity with the annealing suggests an improvement in the flake-to-flake bonding, where stiffer bond would allow a broader phonon spectrum to be transmitted. The difference in enhancement between electrical conductivity and thermal conductivity suggests that the improved bonding reduces the barrier to electron conduction much more so than for phonons.

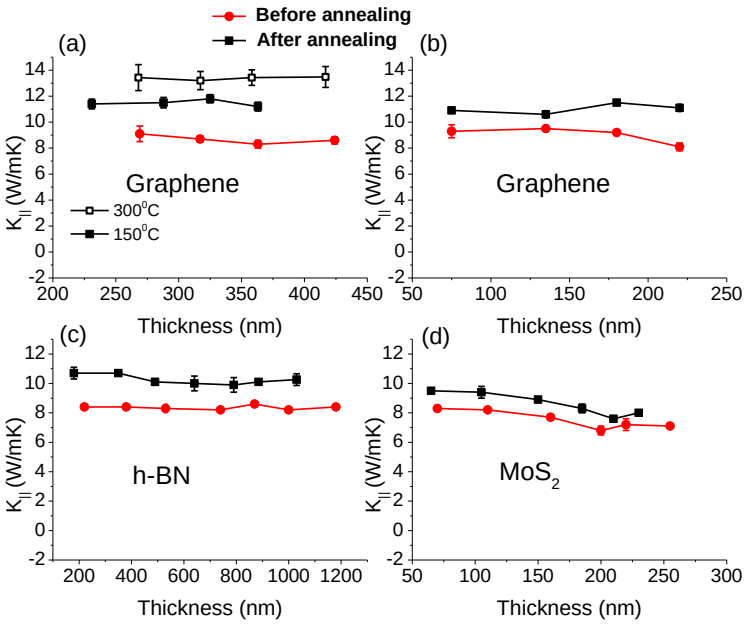

Figure 5. 4 In-plane thermal conductivities of printed films as a function of the thickness before(red) and after annealing(black).

The measured out of plane thermal conductivity of graphene thin film is even lower than predicted from the minimum thermal conductivity model for disordered crystals and also there is no change in out of plane thermal conductivity before and after annealing. The overall out of plane thermal conductivity before annealing is 0.31 $\pm$ 0.02 W/mK ,and 0.30 $\pm$ 0.02 after annealing. The ratio of anisotropy is 22:1 (before annealing), and 36:1 (after annealing).

Then, we conducted direct measurements on similar flake size h-BN thin films over a wide range of thicknesses (180nm-1180nm). Similar to graphene, no thickness dependence on h-BN thin films is observed (Figure 5.4(c)). The average in-plane thermal conductivity of the h-BN thin film is 8.3 ± 0.1 W/mK before annealing and 10.1 ± 0.1

W/mK after annealing at 150^0C. The measured in-plane thermal conductivity of nanometer flake size h-BN ink is about half of the reported in-plane thermal conductivity of h-BN laminate with micron scale flake size[106]. The improvement in thermal conductivity with annealing for h-BN thin film is ~22%. However, the out of plane thermal conductivity of the h-BN film is higher than graphene thin film and the average value is 0.49 ± 0.01 W/mK before annealing and 0.48 ± 0.02 W/mK after annealing. The measured conductivity is also found to be highly anisotropic with a ratio of 17:1 (before annealing) and 21:1 (after annealing).

Finally, we carried out thermal measurements on printed MoS_2 films for various thicknesses. The measured in-plane thermal conductivity as a function of thickness is shown in Figure 5.4(d), and no thickness dependency is observed. The average in-plane thermal conductivity of MoS_2 thin film is 7.8 ± 0.2 W/mK before annealing and 8.8 ± 0.3 W/mK after annealing. To our knowledge, there is no reported thermal conductivity value in the literature to compare to. The measured out of plane thermal conductivity is 0.31 ± 0.02 W/mK before annealing and 0.3 ± 0.01 W/mK after annealing. The improvement in thermal conductivity with annealing is 13% compared to 22% for h-BN, and 35% for graphene and the anisotropic ratio is 17:1 (before annealing) and 21:1 (after annealing). In each case, the error bar represents the confidence interval obtained from several measurements on each line.

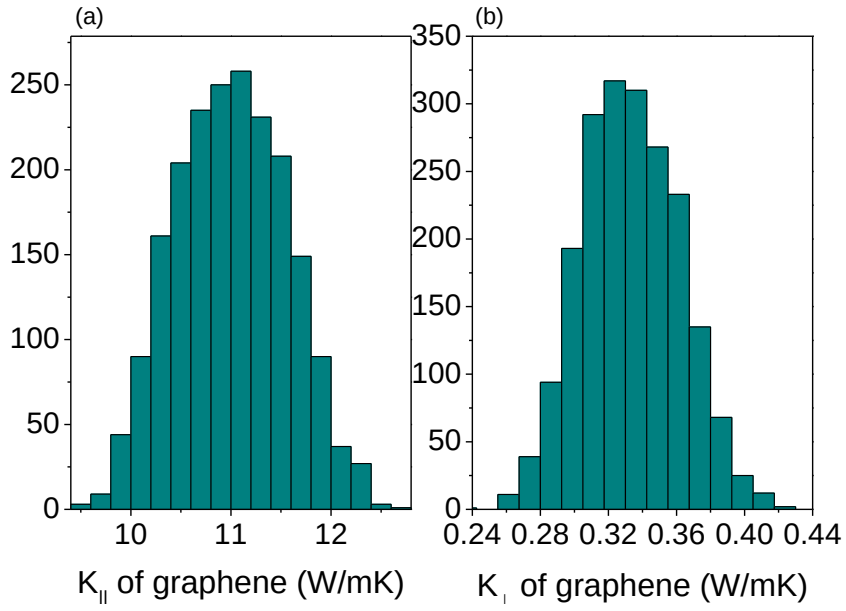

Figure 5. 5 Monte Carlo histogram for annealed graphene thin film ($k_{\parallel} = 11 \pm 0.56$ W/mK and $k_{\perp} = 0.33 \pm 0.03$ W/mK).

In order to estimate the propagation of all possible errors in the input parameters, a robust uncertainty calculation is done in all three samples thorough the Monte Carlo computational method. Nominal input parameters of the diffusive heat model are selected randomly. The parameters are considered to have a normal distribution about its mean value with a standard deviation which is estimated from several independent measurements. The uncertainty in Al thickness is 4%, in plane thermal conductivity of Al 5%, the thickness of the substrate 5%, the thickness of the ink 4%, and RMS spot size 4%. Additionally, the uncertainty in the measured phase originating from the experimental noise of 0.1 degrees is also included. In our model, the volumetric heat capacity of inks is initially considered similar to their bulk value. However, here, we randomly selected the volumetric heat capacity from 85% of the bulk value to the original bulk value. This is

based on the fact that the volumetric heat capacity can be slightly lower than the original bulk value due to the presence of other additives during the time of ink formulations. The effect of volumetric heat capacity in thermal conductivities is comparatively small and lowering the heat capacity slightly reduces the in-plane thermal conductivity and increases the out of plane conductivity. Then using the input parameters, the experimental data are fitted to the diffusive heat equation to extract the fitting parameters that minimize the error between the model and experiment. We repeated the procedure 2000 times until the outcomes converge to a normal distribution. For each Monte Carlo run, both the fitted parameters and goodness of fit were recorded, the latter was used to weigh the value of its associated parameter for statistical significance. We calculated the weighted mean value and the standard deviation. The resulting histograms of in-plane thermal conductivity and out of plane thermal conductivity of the annealed graphene thin film is shown in Figure 5.5. The in-plane thermal conductivity is found as 11 ± 0.56 W/mK , while the out of plane thermal conductivity is 0.33 ± 0.03 W/mK.

In spite of their similar layered structure, these 2D materials have intrinsically different thermal conductivities. Graphene has extremely high in-plane conduction due to the strong sp^2 bonding and relatively small mass of carbon atom. While the in-plane thermal

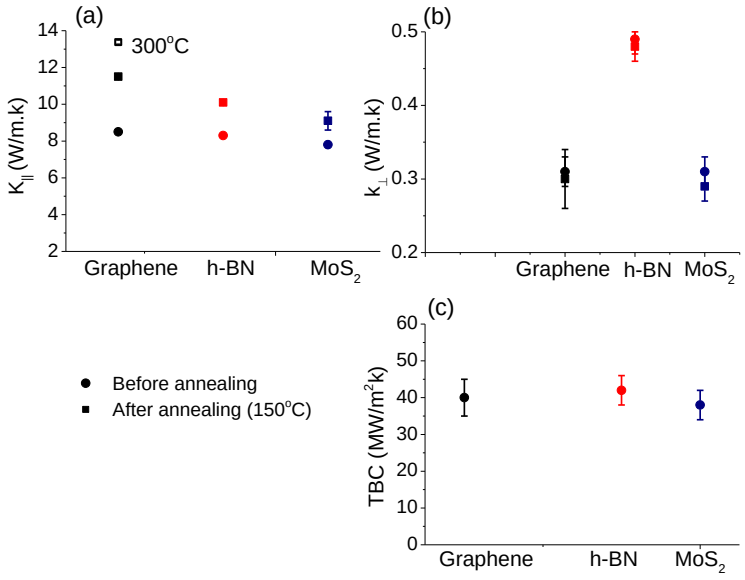

Figure 5. 6 Summarized (a) in plane thermal conductivity, (b) out of plane thermal conductivity, and (c) thermal boundary conductance with Al layer before(circle) and after annealing(rectangle) of graphene(black), h-BN(red), and MoS_2(navy) films.

conductivity of graphene is ~3000 W/mK[24,25] on a suspended geometry and ~1000 W/mK[10,47,84] on a supported geometry at room temperature, the in-plane thermal conductivities of h-BN and MoS_2 are ~350 W/mK[48] and ~85 W/mK[58] respectively. However, the measured in-plane thermal conductivities of printed graphene, h-BN, and MoS_2 films are surprisingly lower than their intrinsic thermal properties and also indistinguishable from each other. The averages in-plane thermal conductivities of these three printed films are shown in Figure 5.6 (a). The similar and overall low $K_{||}$ values of these films indicate that the heat conduction is mainly limited by extrinsic factors such as the flake size and flake to flake attachment, rather than their intrinsic thermal properties.

The flake size dependent thermal conductivity was previously confirmed on the micron-scale size graphene[106] and h-BN laminate[107].

Although the in-plane thermal conductivities of these films are similar, the out of plane thermal conductivities are substantially different. The averages of the out of plane thermal conductivities of these three printed films are shown in Figure 5.6(b). The ultra-low cross-plane conductivities are surprising considering that in the literature a high density of interfaces among dissimilar materials are needed to obtain values below ~1 W/mK[108,109] or an extreme disorder as in the case of amorphous carbons is required to achieve these low values. As an example, an ultralow thermal conductivity of 0.33 W/mK was reported at room temperature in MLs made of Au and Si with a high interfacial density of ~ 0.2 interface/ nm[110]. Here a range of values from ~0.32 W/mK (graphene, MoS2) to 0.47 W/mK (h-BN) are obtained by layering relatively ordered structures which are made of stacked platelets that form a random incommensurate network with very weak Van Der wall bonds, rather than a crystal-like structure.

Since we also have enough sensitivity to TBC with the metallic layer, we also concurrently measured the TBCs of three films with Al. The measured TBCs for these three films are quite low and in line with previously measured Al/bulk graphite[9,10]. This low boundary conductance can be attributed to the factor of five times phonon frequency mismatch between the Al and 2D crystals. The measured TBCs for all three films are shown in Figure 5.6(c).

In order to gain further insight into the heat conduction of these printed films, we theoretically calculated the in-plane thermal conductivity of the graphene film following

the approach of H Malekpour et al.[106]. The in-plane thermal conductivity of graphene is given by:[106]

$$K = K_{x,x} = \frac{1}{L_x L_y L_z} \sum_{s,\vec{q}} \hbar\omega_s(\vec{q})\tau(\omega_s(\vec{q}))\upsilon_{x,s}\upsilon_{x,s}\frac{\partial N_0}{\partial T} \quad (27)$$

where $\tau(\omega_s(\vec{q}))$ is the relaxation time for a phonon with the frequency $\omega_s(\vec{q})$ from the *s*th acoustic phonon branch, *s* = Longitudinal Acoustic (LA), Transverse Acoustic (TA), and Flexural Acoustic/ out of plane Acoustic (ZA), $\vec{q}$ is the three dimensional phonon wave vector, $\upsilon_{x,s}$ is the projection of phonon group velocity, $N_0 = \frac{1}{(\exp[\frac{\hbar\omega_s}{K_B T}]-1)}$ is the Bose-Einstein distribution function, $L_x, L_y, \ and \ L_z$ are the sizes of the sample, $\hbar$ is the reduced Plank constant, and *T* is temperature.

The phonon transport in graphene layer is two dimensional for phonons with frequencies $\omega_s > \omega_{c,s}$ and three dimensional for phonons with frequencies $\omega_s \leq \omega_{c,s}$[106] , where ω_c is low-bound cut-off frequency, $\upsilon_s{}^{\perp} = \frac{\omega_{c,s}}{q_{z,max}}$ is the projection of group velocity of *s*th phonon branch, and $\omega_{c,s}$ is the phonon frequency of *s*th branch at the A-point of the graphite Brillouin zone. Equation 27 can be rewritten for the 2-dimensional and 3-dimensional parts as below[106]

$$K^{3D} \equiv \frac{\hbar^2}{4\pi^2 K_B T^2} \sum_{s=LA,TA,ZA} \frac{1}{{v_s}^{\perp}} \int_0^{\omega_{c,s}} [{\omega_s}^{\parallel}(q_{\parallel})]^3 \ \tau({\omega_s}^{\parallel})({v_s}^{\parallel})(q_{\parallel})) \frac{\exp\left(\frac{\hbar{\omega_s}^{\parallel}}{K_B T}\right)}{[\exp\left(\frac{\hbar{\omega_s}^{\parallel}}{K_B T}\right) - 1]^2} q_{\parallel} d{\omega_s}^{\parallel} \quad 28)$$

$$K^{2D} = \frac{\hbar^2}{4\pi^2 K_B T^2} \sum_{s=LA,TA,ZA} \frac{\omega_{c,s}}{{v_s}^{\perp}} \int_{\omega_{c,s}}^{\omega_{max,s}} [{\omega_s}^{\parallel}(q_{\parallel})]^2 \ \tau({\omega_s}^{\parallel})({v_s}^{\parallel})(q_{\parallel})) \frac{\exp\left(\frac{\hbar{\omega_s}^{\parallel}}{K_B T}\right)}{[\exp\left(\frac{\hbar{\omega_s}^{\parallel}}{K_B T}\right) - 1]^2} q_{\parallel} d{\omega_s}^{\parallel} \quad 29)$$

Figure 5.7(a) shows the calculated thermal conductivity of graphene film as a function of defect scattering strength (Γ) for several flake sizes. The dashed lines consider two phonon scattering mechanisms: Umklapp scattering ($\tau_U({\omega_s}^{\parallel}) = \frac{M{v_s}^2\omega_{max,s}}{\gamma_s^2 K_B T[{\omega_s}^{\parallel}]^2)}$) and flake boundary scattering ($\tau_b({\omega_s}^{\parallel}) = \frac{D}{{v_s}^{\parallel}}$,) whereas solid lines also include point defect scattering ($\tau_{pd}({\omega_s}^{\parallel}) = \frac{4{v_s}^{\parallel}}{S_0 \Gamma q[{\omega_s}^{\parallel}]^2}$) into consideration which has a much stronger effect. Here, $\gamma_{LA} = 2, \gamma_{TA} = 1,$ and γ_{ZA}= -1.5 are the branch-dependent average Gruneisen parameters, ω_{max} is the maximal frequency of the *s*th branch, S_0 is the cross-section area per atom, and *M* is the graphene unit cell mass. The total phonon relaxation time τ was calculated from the Matthiessen's rule: $\frac{1}{\tau} = \frac{1}{\tau_U} + \frac{1}{\tau_b} + \frac{1}{\tau_{pd}}$.

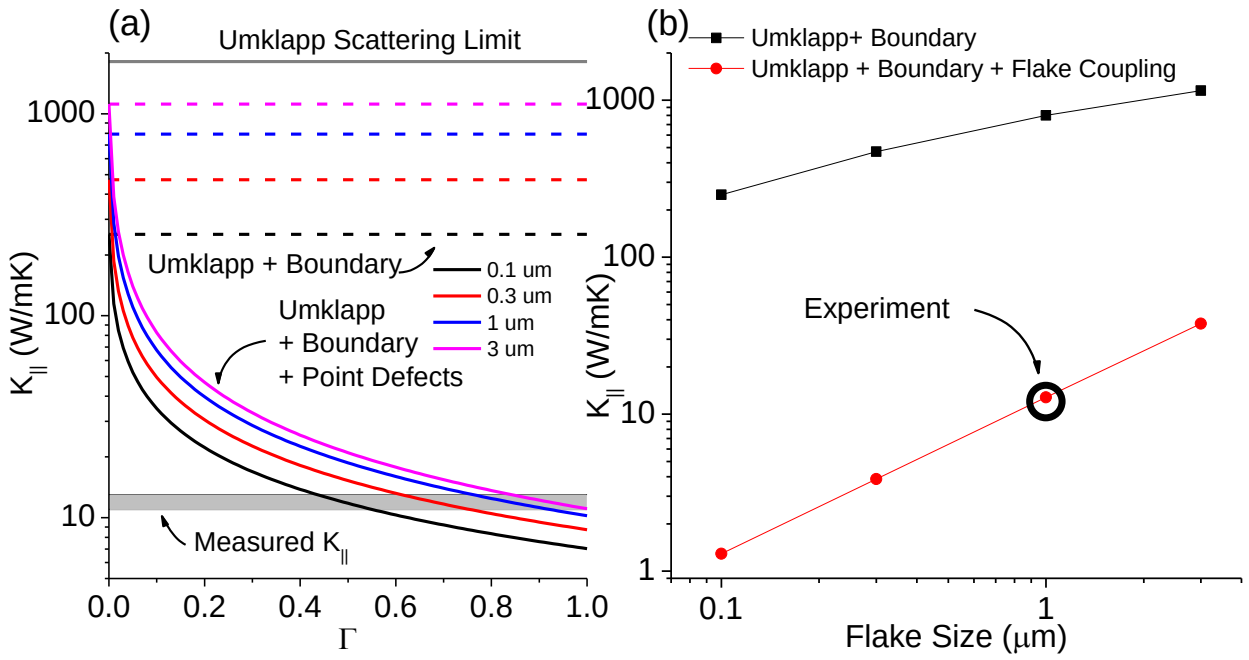

Figure 5. 7 Calculated thermal conductivity as a function of (a) defect scattering strength Γ for several flake sizes (b) flake size.

For all the printed films the accepted value of Γ is ≤0.1 based on elemental analysis of any potential impurities, which leads to an in plane thermal conductivity of ~60 W/mK for a 1-micron sized flake. Hence, for inter-flake $K_{||}$ to reduce to the measured values, a very large scattering would be needed which is not plausible, and thus the intrinsic $K_{||}$ seems irrelevant to the overall observed value. This is also confirmed by the similarly low thermal conductivities measured for these three printed films despite having distinct and very high

intrinsic conductivities in their layered form. The black curve in Figure 5.7 (b) shows the calculated thermal conductivity as a function of flake size considering Umklapp and boundary scattering. Since these printed films are in ink form, flake to flake attachment is crucial but it has not been taken into account in the model description by H Malekpour et al. for graphene laminate[106]. We included flake coupling in the model by assuming that on average a TBC is inserted in series after every flake, obtaining the red curve in Figure 5.7 (b). Adding an intra-flake conductance of 14 MW/m^{2}K, as previously determined[111], yields a reasonable agreement with the measured conductivity. A similar value for intra-flake conductance of 15 MW/m^{2}K has also been recently reported[112]. Thus, the measured in-plane thermal conductivity of graphene film is independent of its intrinsic property and limited by flake size and more so by flake coupling.

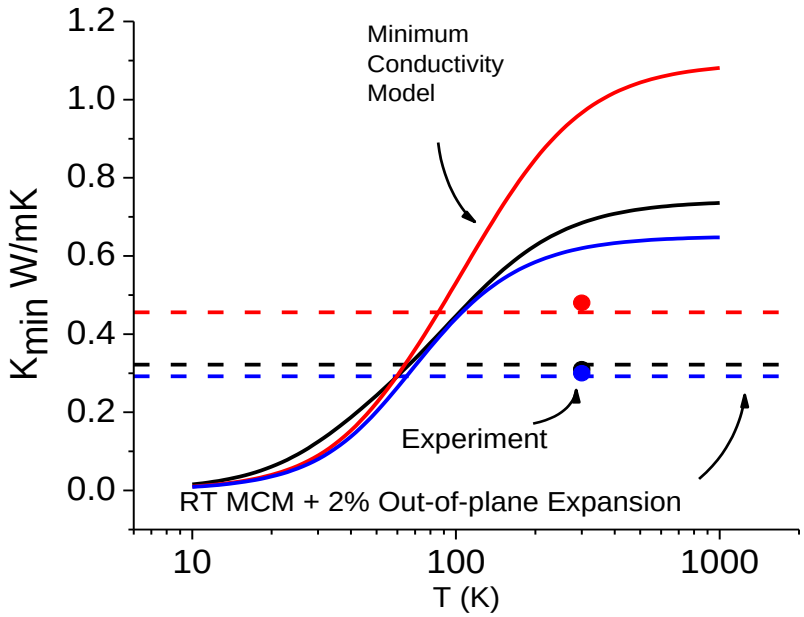

Figure 5. 8 Minimum out of plane thermal conductivities of graphite(black), h-BN(red), and MoS_2(blue) as a function of temperature.

The measured out of plane thermal conductivities are extremely low. To gain confidence in our experimental measurements, we then compared the measured out of plane thermal conductivities with predicted thermal conductivities for three printed films using the minimum thermal conductivity model (MCM)[113]. The minimum thermal conductivity is defined as[113]

$$\Lambda_{min} = \left(\frac{\pi}{6}\right)^{1/3} K_B n^{2/3} \sum_i V_i \left(\frac{T}{\theta_i}\right)^2 \int_0^{\frac{\theta_i}{T}} \frac{x^3 e^x}{(e^x - 1)^2} dx \quad (30)$$

Here, the sum is taken over three sound modes (two transverse and one longitudinal) with sound speed V_i, and $\theta_i = V_i \left(\frac{\hbar}{K_B}\right)(6\pi^2 n)^{1/3}$, where *n* is the number density of atoms.

This model yields the minimum conductivity in the extreme disorder limit, which is a reasonable starting point for the incommensurate stacking in the films. The solid lines in Figure 5.8 show the minimum thermal conductivities as a function of temperature for graphite, h-BN, and MoS_2, which are still higher than the experimentally measured values. In the ink form, expansion in layer spacing is expected to take place due to the presence of residual surfactants. The relative out of plane thermal conductivity as a function of average expansion μ is given by[114]

$$\frac{< K >_\mu}{K_0} = \frac{1 - a\mu}{1 + \mu/(1 - a\mu)} \quad (31)$$

where *a* = 25.5 is the fitting parameter. This dependence was derived from first principle studies of 2D crystals with incommensurate stacking. The dashed lines depict the reduction in the room temperature minimum thermal conductivities values by taking a 2% out of plane expansion into account, and this amount of increase in flake spacing

recovers the experimental data. Thus, the reduction of out of plane thermal conductivity is mainly due to the expansion in layer spacing and stacking disorder. Remember stacking disorder is the starting point for the MCM. Here, we are referring to the small effect of staking disorder observed by first principles, but we are not discussing this here. A very recent theoretical study has also confirmed that a 2% lattice expansion explains the experiments performed on similar layered compound[114].

5.5 Summary

We have investigated the thermal properties of graphene, h-BN, and MoS_2 films produced by ink-jet printing of water-based 2D-materials inks. The measured thermal conductivities are independent of thickness and intrinsic thermal properties, and are very anisotropic with a ratio of about 20-35:1. The value of the measured in-plane thermal conductivities of these films are very close to each other, and it was determined both theoretically and experimentally that the in-plane thermal conductivity is mainly limited by flake size and flake coupling. The measured value of the out of plane thermal conductivity of graphene film was found to be extremely low, in fact lower than any other crystalline carbon. The out of plane thermal conductivity is then theoretically confirmed to be affected by random flake stacking and interstitial molecules. The electrical and thermal conductivities of these printed films are not strongly correlated. The measured electrical and thermal conductivities will be very useful for the development of electronic and optoelectronic devices produced by inkjet printing.

CHAPTER 6

Conclusion and Outlook

6.1 Summary of the thesis

Optical pump-probe techniques are well recognized for the direct measurements of the thermal properties of thin films and bulk materials such as thermal conductivity and thermal boundary conductance (TBC). However, typically these techniques are not sensitive to in-plane heat transport. Although anisotropic materials are attractive for a wide range of device applications due to their distinct properties, measuring anisotropic thermal properties of these materials are challenging because of the low sensitivity to lateral heat transport. The study and characterization of heat transport on anisotropic materials can solve the heat dissipation problem on emerging devices based on these materials. Hence, it is necessary to measure directly the anisotropic thermal conductivity, and thermal boundary conductance simultaneously.

In chapter 2, I explained the theoretical modeling and experimental setup with all the optics required to carry out measurements through frequency domain thermoreflectance technique to measure the thermal properties of thin films and interfaces. FDTR has several advantages over TDTR. A small RMS laser spot size allows us to go to a very high modulation frequency of up to ~100MHz without incorporating other complicated techniques allowing the study of thin materials and non-diffusive transport. Chapter 3 presents the extension of FDTR to beam offset FDTR which enhances the sensitivity to in-plane heat transport. Through beam offset-FDTR we have

measured the anisotropic thermal properties of a range of materials, including single layer graphene on SiO_2, which is promising for novel electronic devices. Measuring thermal properties of 2D layered materials, mainly single and few layers requires further enhancement in sensitivity. To measure the anisotropic thermal properties of 2D layered materials including single and few layers, we have implemented frequency domain magneto-optical Kerr effect which is described in chapter 4. Applying this approach, we have measured the thermal properties of a range of 2-dimensional layered materials including single-layer graphene, few-layer h-BN, single and two-layer MoS_2, and bulk single crystal $MoSe_2$ and single crystal WS_2 which are of also great interest for emerging device applications. Furthermore, over the last few years, solution-processed 2D materials have shown promises due to the ease and low-cost of fabrication. Chapter 5 illustrates the simultaneous measurements of anisotropic thermal conductivity and thermal boundary conductance (TBC) of graphene, h-BN, and MoS_2 thin films produced by ink-jet printing of water-based 2D-material inks. We also observed ultra-low cross-plane thermal conductivities much below 0.5 W/mK in these printed films, even smaller than predicted from the minimum thermal conductivity model. The effect of annealing is observed in these films at different temperatures.

6.2 Outlook

The work in this thesis has contributed to the study of anisotropic thermal transport in nanoscale materials and devices through the development of extended experimental tools and measurements. The extended techniques will help investigate the thermal properties of anisotropic materials, composite and devices more accurately with enhanced sensitivity. It will be now more accessible to measure the thermal properties of polymer nanocomposites using these techniques which are highly anisotropic in nature and promising for thermoelectric applications. The transducer thickness can be decreased to ~10 nm, which further enhances the sensitivity to lateral heat transport. In addition to that, reducing the laser spot has helped reach higher modulation frequency and lead to the study of non-diffusive phenomena efficiently. The thermal and electrical measurements on printed films made of 2D materials based inks would help develop applications based on the thermal and electrical properties of these materials. In short, the developed techniques in this thesis will be essential tools to characterize anisotropic materials which can improve the efficiency of electronic devices based on these novel materials.

REFERENCES

1. Chen, G. *Nanoscale Energy Transport and Conversion: A Parallel Treatment of Electrons, Molecules, Phonons, and Photons*. (Oxford University Press, 2005).
2. Cahill, D. G. *et al.* Nanoscale thermal transport. *Journal of Applied Physics* **93**, 793–818 (2002).
3. Cahill, D. G. *et al.* Nanoscale thermal transport. II. 2003–2012. *Applied Physics Reviews* **1**, 011305 (2014).
4. Chen, Z.-G., Han, G., Yang, L., Cheng, L. & Zou, J. Nanostructured thermoelectric materials: Current research and future challenge. *Progress in Natural Science: Materials International* **22**, 535–549 (2012).
5. Cahill, D. G. Thermal conductivity measurement from 30 to 750 K: the 3ω method. *Review of Scientific Instruments* **61**, 802–808 (1990).
6. Cahill, D. G. Analysis of heat flow in layered structures for time-domain thermoreflectance. *Review of Scientific Instruments* **75**, 5119–5122 (2004).
7. Feser, J. P. & Cahill, D. G. Probing anisotropic heat transport using time-domain thermoreflectance with offset laser spots. *Review of Scientific Instruments* **83**, 104901 (2012).
8. Yang, J., Maragliano, C. & Schmidt, A. J. Thermal property microscopy with frequency domain thermoreflectance. *Review of Scientific Instruments* **84**, 104904 (2013).
9. Schmidt, A. J., Chen, X. & Chen, G. Pulse accumulation, radial heat conduction, and anisotropic thermal conductivity in pump-probe transient thermoreflectance. *Review of Scientific Instruments* **79**, 114902 (2008).

10. Rahman, M. *et al.* Measuring the thermal properties of anisotropic materials using beam-offset frequency domain thermoreflectance. *Journal of Applied Physics* **123**, 245110 (2018).
11. Withers, F. *et al.* Heterostructures Produced from Nanosheet-Based Inks. *Nano Letters* **14**, 3987–3992 (2014).
12. Hu, G. *et al.* Functional inks and printing of two-dimensional materials. *Chemical Society Reviews* **47**, 3265–3300 (2018).
13. McManus, D. *et al.* Water-based and biocompatible 2D crystal inks for all-inkjet-printed heterostructures. *Nature Nanotechnology* **12**, 343–350 (2017).
14. Ng, L. W. T. *et al. Printing of Graphene and Related 2D Materials: Technology, Formulation and Applications*. (Springer, 2018).
15. POLLACK, G. L. Kapitza Resistance. *Rev. Mod. Phys.* **41**, 48–81 (1969).
16. Lyeo, H.-K. & Cahill, D. G. Thermal conductance of interfaces between highly dissimilar materials. *Phys. Rev. B* **73**, 144301 (2006).
17. Wilson, R. B. & Cahill, D. G. Experimental Validation of the Interfacial Form of the Wiedemann-Franz Law. *Phys. Rev. Lett.* **108**, 255901 (2012).
18. Swartz, E. T. & Pohl, R. O. Thermal boundary resistance. *Rev. Mod. Phys.* **61**, 605–668 (1989).
19. Duda, J. C., Smoyer, J. L., Norris, P. M. & Hopkins, P. E. Extension of the diffuse mismatch model for thermal boundary conductance between isotropic and anisotropic materials. *Appl. Phys. Lett.* **95**, 031912 (2009).

20. Zhao, D., Qian, X., Gu, X., Jajja, S. A. & Yang, R. Measurement Techniques for Thermal Conductivity and Interfacial Thermal Conductance of Bulk and Thin Film Materials. *J. Electron. Packag* **138**, 040802-040802–19 (2016).
21. Malekpour, H. & Balandin, A. A. Raman Optothermal Technique for Measuring Thermal Conductivity of Graphene and Related Materials. *Journal of Raman Spectroscopy* **49**, 106–120 (2018).
22. Regner, K. T., Majumdar, S. & Malen, J. A. Instrumentation of broadband frequency domain thermoreflectance for measuring thermal conductivity accumulation functions. *Review of Scientific Instruments* **84**, 064901 (2013).
23. Schmidt, A. J., Cheaito, R. & Chiesa, M. A frequency-domain thermoreflectance method for the characterization of thermal properties. *Review of Scientific Instruments* **80**, 094901 (2009).
24. Balandin, A. A. Thermal properties of graphene and nanostructured carbon materials. *Nature Materials* **10**, 569–581 (2011).
25. Ghosh, S. *et al.* Extremely high thermal conductivity of graphene: Prospects for thermal management applications in nanoelectronic circuits. *Appl. Phys. Lett.* **92**, 151911 (2008).
26. Bae, M.-H. *et al.* Ballistic to diffusive crossover of heat flow in graphene ribbons. *Nature Communications* **4**, 1734 (2013).
27. Nika, D. L., Pokatilov, E. P., Askerov, A. S. & Balandin, A. A. Phonon thermal conduction in graphene: Role of Umklapp and edge roughness scattering. *Physical Review B* **79**, (2009).

28. Li, M., Kang, J. S. & Hu, Y. Anisotropic thermal conductivity measurement using a new Asymmetric-Beam Time-Domain Thermoreflectance (AB-TDTR) method. *Review of Scientific Instruments* **89**, 084901 (2018).
29. Shen, S., Henry, A., Tong, J., Zheng, R. & Chen, G. Polyethylene nanofibres with very high thermal conductivities. *Nature Nanotechnology* **5**, 251–255 (2010).
30. Slack, G. A. Anisotropic Thermal Conductivity of Pyrolytic Graphite. *Phys. Rev.* **127**, 694–701 (1962).
31. Parker, W. J., Jenkins, R. J., Butler, C. P. & Abbott, G. L. Flash Method of Determining Thermal Diffusivity, Heat Capacity, and Thermal Conductivity. *Journal of Applied Physics* **32**, 1679–1684 (1961).
32. Golombok, M. & Shirvill, L. C. Laser flash thermal conductivity studies of porous metal fiber materials. *Journal of Applied Physics* **63**, 1971–1976 (1988).
33. Mishra, V., Hardin, C. L., Garay, J. E. & Dames, C. A 3 omega method to measure an arbitrary anisotropic thermal conductivity tensor. *Review of Scientific Instruments* **86**, 054902 (2015).
34. Novoselov, K. S. *et al.* A roadmap for graphene. *Nature* **490**, 192–200 (2012).
35. Novoselov, K. S., Mishchenko, A., Carvalho, A. & Neto, A. H. C. 2D materials and van der Waals heterostructures. *Science* **353**, aac9439 (2016).
36. Geim, A. K. & Grigorieva, I. V. Van der Waals heterostructures. *Nature* **499**, 419–425 (2013).
37. Withers, F. *et al.* Light-emitting diodes by band-structure engineering in van der Waals heterostructures. *Nature Materials* **14**, 301–306 (2015).

38. Yankowitz, M., Xue, J. & LeRoy, B. J. Graphene on hexagonal boron nitride. *J. Phys.: Condens. Matter* **26**, 303201 (2014).
39. Zhang, Z., Hu, S., Chen, J. & Li, B. Hexagonal boron nitride: a promising substrate for graphene with high heat dissipation. *Nanotechnology* **28**, 225704 (2017).
40. Choi, W. *et al.* Recent development of two-dimensional transition metal dichalcogenides and their applications. *Materials Today* **20**, 116–130 (2017).
41. Tian, T., Rice, P., Santos, E. J. G. & Shih, C.-J. Multiscale Analysis for Field-Effect Penetration through Two-Dimensional Materials. *Nano Lett.* **16**, 5044–5052 (2016).
42. Mak, K. F., Lee, C., Hone, J., Shan, J. & Heinz, T. F. Atomically Thin ${\mathrm{MoS}}_{2}$: A New Direct-Gap Semiconductor. *Phys. Rev. Lett.* **105**, 136805 (2010).
43. Zhao, Y., Wang, W., Li, C. & He, L. First-principles study of nonmetal doped monolayer MoSe 2 for tunable electronic and photocatalytic properties. *Scientific Reports* **7**, 17088 (2017).
44. Jung, C. *et al.* Highly Crystalline CVD-grown Multilayer $MoSe_2$ Thin Film Transistor for Fast Photodetector. *Scientific Reports* **5**, 15313 (2015).
45. Shim, G. W. *et al.* Large-Area Single-Layer MoSe2 and Its van der Waals Heterostructures. *ACS Nano* **8**, 6655–6662 (2014).
46. Peimyoo, N. *et al.* Thermal conductivity determination of suspended mono- and bilayer WS2 by Raman spectroscopy. *Nano Res.* **8**, 1210–1221 (2015).
47. Yang, J. *et al.* Thermal conductance imaging of graphene contacts. *Journal of Applied Physics* **116**, 023515 (2014).

48. Sichel, E. K., Miller, R. E., Abrahams, M. S. & Buiocchi, C. J. Heat capacity and thermal conductivity of hexagonal pyrolytic boron nitride. *Phys. Rev. B* **13**, 4607–4611 (1976).
49. Farzaneh, M. *et al.* CCD-based thermoreflectance microscopy: principles and applications. *Journal of Physics D: Applied Physics* **42**, 143001 (2009).
50. Feldman., A. , High Temp. - High Press. 31, 293 (1999).
51. Hopkins, P. E. *et al.* Criteria for Cross-Plane Dominated Thermal Transport in Multilayer Thin Film Systems During Modulated Laser Heating. *J. Heat Transfer* **132**, 081302-081302–10 (2010).
52. Belliard, L. *et al.* Determination of the thermal diffusivity of bulk and layered samples by time domain thermoreflectance: Interest of lateral heat diffusion investigation in nanoscale time range. *Journal of Applied Physics* **117**, 065306 (2015).
53. Wilson, R. B. & Cahill, D. G. Anisotropic failure of Fourier theory in time-domain thermoreflectance experiments. *Nature Communications* **5**, 5075 (2014).
54. Hua, C., Chen, X., Ravichandran, N. K. & Minnich, A. J. Experimental metrology to obtain thermal phonon transmission coefficients at solid interfaces. *Phys. Rev. B* **95**, 205423 (2017).
55. Yang, J., Ziade, E. & Schmidt, A. J. Uncertainty analysis of thermoreflectance measurements. *Review of Scientific Instruments* **87**, 014901 (2016).
56. Sun, Z., Martinez, A. & Wang, F. Optical modulators with 2D layered materials. *Nature Photonics* **10**, 227 (2016).
57. Luo, Z. *et al.* Anisotropic in-plane thermal conductivity observed in few-layer black phosphorus. *Nature Communications* **6**, 8572 (2015).

58. Liu, J., Choi, G.-M. & Cahill, D. G. Measurement of the anisotropic thermal conductivity of molybdenum disulfide by the time-resolved magneto-optic Kerr effect. *Journal of Applied Physics* **116**, 233107 (2014).
59. Schmidt, A. J., Collins, K. C., Minnich, A. J. & Chen, G. Thermal conductance and phonon transmissivity of metal–graphite interfaces. *Journal of Applied Physics* **107**, 104907 (2010).
60. Freitag, M. *et al.* Energy Dissipation in Graphene Field-Effect Transistors. *Nano Lett.* **9**, 1883–1888 (2009).
61. Liao, A. D. *et al.* Thermally Limited Current Carrying Ability of Graphene Nanoribbons. *Phys. Rev. Lett.* **106**, 256801 (2011).
62. Bae, M.-H., Ong, Z.-Y., Estrada, D. & Pop, E. Imaging, Simulation, and Electrostatic Control of Power Dissipation in Graphene Devices. *Nano Lett.* **10**, 4787–4793 (2010).
63. Rodin, D. & Yee, S. K. Simultaneous measurement of in-plane and through-plane thermal conductivity using beam-offset frequency domain thermoreflectance. *Review of Scientific Instruments* **88**, 014902 (2017).
64. Shahzadeh, M., Rahman, M., Hellwig, O. & Pisana, S. High-frequency measurements of thermophysical properties of thin films using a modified broad-band frequency domain thermoreflectance approach. *Review of Scientific Instruments* **89**, 084905 (2018).
65. Braeuninger-Weimer, P., Brennan, B., Pollard, A. J. & Hofmann, S. Understanding and Controlling Cu-Catalyzed Graphene Nucleation: The Role of Impurities, Roughness, and Oxygen Scavenging. *Chem. Mater.* **28**, 8905–8915 (2016).

66. Hua, C. & Minnich, A. J. Heat dissipation in the quasiballistic regime studied using the Boltzmann equation in the spatial frequency domain. *Phys. Rev. B* **97**, 014307 (2018).
67. Buyco, E. H. & Davis, F. E. Specific heat of aluminum from zero to its melting temperature and beyond. Equation for representation of the specific heat of solids. *J. Chem. Eng. Data* **15**, 518–523 (1970).
68. DeSorbo, W. & Tyler, W. W. The Specific Heat of Graphite from 13° to 300°K. *J. Chem. Phys.* **21**, 1660–1663 (1953).
69. Horbach, J., Kob, W. & Binder, K. Specific Heat of Amorphous Silica within the Harmonic Approximation. *J. Phys. Chem. B* **103**, 4104–4108 (1999).
70. Glazov, V. M. & Pashinkin, A. S. The Thermophysical Properties (Heat Capacity and Thermal Expansion) of Single-Crystal Silicon. *High Temperature* **39**, 413–419 (2001).
71. Ditmars, D. A., Ishihara, S., Chang, S. S., Bernstein, G. & West, E. D. Enthalpy and Heat-Capacity Standard Reference Material: Synthetic Sapphire (Alpha-Al2O3) From 10 to 2250 K. *Journal of Research of the National Bureau of Standards* **87**, 159 (1982).
72. Slack, G. A. Thermal Conductivity of Pure and Impure Silicon, Silicon Carbide, and Diamond. *Journal of Applied Physics* **35**, 3460–3466 (1964).
73. HOPG Advanced Ceramics Brand Grade ZYA, 12x12x2 mm Thick, Package of 1 Piece | 430HP-AB | SPI Supplies. Available at: https://www.2spi.com/item/430hp-ab/hopg-momentive-performance./. (Accessed: 17th March 2019)
74. Burghartz, S. & Schulz, B. Thermophysical properties of sapphire, AlN and MgAl2O4 down to 70 K. *Journal of Nuclear Materials* **212**–**215**, 1065–1068 (1994).
75. Dobrovinskaya, E. R., Lytvynov, L. A. & Pishchik, V. *Sapphire: Material, Manufacturing, Applications*. (Springer Science & Business Media, 2009).

76. Winey, J. M., Gupta, Y. M. & Hare, D. E. r-axis sound speed and elastic properties of sapphire single crystals. *Journal of Applied Physics* **90**, 3109–3111 (2001).
77. Malen, J. A. *et al.* Optical Measurement of Thermal Conductivity Using Fiber Aligned Frequency Domain Thermoreflectance. *J. Heat Transfer* **133**, 081601-081601–7 (2011).
78. Zhang, C. *et al.* Heat conduction across metal and nonmetal interface containing imbedded graphene layers. *Carbon* **64**, 61–66 (2013).
79. Koh, Y. K., Bae, M.-H., Cahill, D. G. & Pop, E. Heat Conduction across Monolayer and Few-Layer Graphenes. *Nano Lett.* **10**, 4363–4368 (2010).
80. Mak, K. F., Lui, C. H. & Heinz, T. F. Measurement of the thermal conductance of the graphene/SiO2 interface. *Appl. Phys. Lett.* **97**, 221904 (2010).
81. Seol, J. H. *et al.* Two-Dimensional Phonon Transport in Supported Graphene. *Science* **328**, 213–216 (2010).
82. Cai, W. *et al.* Thermal Transport in Suspended and Supported Monolayer Graphene Grown by Chemical Vapor Deposition. *Nano Lett.* **10**, 1645–1651 (2010).
83. Lee, J.-U., Yoon, D., Kim, H., Lee, S. W. & Cheong, H. Thermal conductivity of suspended pristine graphene measured by Raman spectroscopy. *Phys. Rev. B* **83**, 081419 (2011).
84. Pisana, S., Rahman, M., Shahzadeh, M. Frequency-Domain Magneto-Optical Kerr Effect for thermal property measurements of anisotropic 2-dimensional materials. in *Bulletin of the American Physical Society* (American Physical Society), March, 2019.
85. Wang, Y., Xu, N., Li, D. & Zhu, J. Thermal Properties of Two Dimensional Layered Materials. *Advanced Functional Materials* **27**, 1604134 (2017).

86. Casiraghi, C., Pisana, S., Novoselov, K. S., Geim, A. K. & Ferrari, A. C. Raman fingerprint of charged impurities in graphene. *Appl. Phys. Lett.* **91**, 233108 (2007).
87. Ferrari, A. C. *et al.* Raman Spectrum of Graphene and Graphene Layers. *Phys. Rev. Lett.* **97**, 187401 (2006).
88. Ghosh, R. *et al.* Large area chemical vapor deposition growth of monolayer MoSe2 and its controlled sulfurization to MoS2. *Journal of Materials Research* **31**, 917–922 (2016).
89. Lee, C. *et al.* Anomalous Lattice Vibrations of Single- and Few-Layer MoS2. *ACS Nano* **4**, 2695–2700 (2010).
90. Li, H. *et al.* From Bulk to Monolayer MoS2: Evolution of Raman Scattering. *Advanced Functional Materials* **22**, 1385–1390 (2012).
91. Berkdemir, A. *et al.* Identification of individual and few layers of WS_2 using Raman Spectroscopy. *Scientific Reports* **3**, 1755 (2013).
92. Stenger, I. *et al.* Low frequency Raman spectroscopy of few-atomic-layer thick hBN crystals. *2D Mater.* **4**, 031003 (2017).
93. Cheaito, R. *et al.* Thermal boundary conductance accumulation and interfacial phonon transmission: Measurements and theory. *Phys. Rev. B* **91**, 035432 (2015).
94. Oommen. S.M., Pisana, S. Tuning the thermal boundary conductance at metal-dielectric interfaces by varying interlayer thicknesses. in *Bulletin of the American Physical Society* (American Physical Society), March, 2019.
95. Zobeiri, H. *et al.* Frequency-domain energy transport state-resolved Raman for measuring the thermal conductivity of suspended nm-thick MoSe2. *International Journal of Heat and Mass Transfer* **133**, 1074–1085 (2019).

96. Lindroth, D. O. & Erhart, P. Thermal transport in van der Waals solids from first-principles calculations. *Phys. Rev. B* **94**, 115205 (2016).

97. Chen, Z., Wei, Z., Chen, Y. & Dames, C. Anisotropic Debye model for the thermal boundary conductance. *Phys. Rev. B* **87**, 125426 (2013).

98. Gu, X. & Yang, R. Phonon transport in single-layer transition metal dichalcogenides: A first-principles study. *Appl. Phys. Lett.* **105**, 131903 (2014).

99. Regner, K. T. *et al.* Broadband phonon mean free path contributions to thermal conductivity measured using frequency domain thermoreflectance. *Nature Communications* **4**, 1640 (2013).

100. Regner, K. T., Wei, L. C. & Malen, J. A. Interpretation of thermoreflectance measurements with a two-temperature model including non-surface heat deposition. *Journal of Applied Physics* **118**, 235101 (2015).

101. Jo, I. *et al.* Thermal Conductivity and Phonon Transport in Suspended Few-Layer Hexagonal Boron Nitride. *Nano Lett.* **13**, 550–554 (2013).

102. Zhou, H. *et al.* High thermal conductivity of suspended few-layer hexagonal boron nitride sheets. *Nano Res.* **7**, 1232–1240 (2014).

103. Zhang, X. *et al.* Measurement of Lateral and Interfacial Thermal Conductivity of Single- and Bilayer MoS2 and MoSe2 Using Refined Optothermal Raman Technique. *ACS Appl. Mater. Interfaces* **7**, 25923–25929 (2015).

104. Gu, X., Li, B. & Yang, R. Layer thickness-dependent phonon properties and thermal conductivity of MoS2. *Journal of Applied Physics* **119**, 085106 (2016).

105. Rahman, M., Parvez, K., Dun, C., Casiraghi, C., Pisana, S. Anisotropic thermal conductivity of printed films made of 2D-materials based inks. in *Bulletin of the American Physical Society* (American Physical Society), March 2019.

106. Malekpour, H. *et al.* Thermal Conductivity of Graphene Laminate. *Nano Lett.* **14**, 5155–5161 (2014).

107. Zheng, J.-C. *et al.* High thermal conductivity of hexagonal boron nitride laminates. *2D Mater.* **3**, 011004 (2016).

108. Ong, W.-L., Rupich, S. M., Talapin, D. V., McGaughey, A. J. H. & Malen, J. A. Surface chemistry mediates thermal transport in three-dimensional nanocrystal arrays. *Nature Materials* **12**, 410–415 (2013).

109. Costescu, R. M., Cahill, D. G., Fabreguette, F. H., Sechrist, Z. A. & George, S. M. Ultra-Low Thermal Conductivity in W/Al2O3 Nanolaminates. *Science* **303**, 989–990 (2004).

110. Dechaumphai, E. *et al.* Ultralow Thermal Conductivity of Multilayers with Highly Dissimilar Debye Temperatures. *Nano Lett.* **14**, 2448–2455 (2014).

111. Konatham, D., Papavassiliou, D. V. & Striolo, A. Thermal boundary resistance at the graphene–graphene interface estimated by molecular dynamics simulations. *Chemical Physics Letters* **527**, 47–50 (2012).

112. Estrada, D. *et al.* Thermal transport in layer-by-layer assembled polycrystalline graphene films. *npj 2D Materials and Applications* **3**, 10 (2019).

113. Cahill, D. G., Watson, S. K. & Pohl, R. O. Lower limit to the thermal conductivity of disordered crystals. *Phys. Rev. B* **46**, 6131–6140 (1992).

114. Erhart, P., Hyldgaard, P. & Lindroth, D. O. Microscopic Origin of Thermal Conductivity Reduction in Disordered van der Waals Solids. *Chem. Mater.* **27**, 5511–5518 (2015).